



Advanced Photonics: Science, Technologies and Applications

**Erich Ippen
MASSACHUSETTS INSTITUTE OF TECHNOLOGY**

**07/30/2018
Final Report**

DISTRIBUTION A: Distribution approved for public release.

**Air Force Research Laboratory
AF Office Of Scientific Research (AFOSR)/ RTB1
Arlington, Virginia 22203
Air Force Materiel Command**

DISTRIBUTION A: Distribution approved for public release.

REPORT DOCUMENTATION PAGE

Form Approved
OMB No. 0704-0188

The public reporting burden for this collection of information is estimated to average 1 hour per response, including the time for reviewing instructions, searching existing data sources, gathering and maintaining the data needed, and completing and reviewing the collection of information. Send comments regarding this burden estimate or any other aspect of this collection of information, including suggestions for reducing the burden, to Department of Defense, Washington Headquarters Services, Directorate for Information Operations and Reports (0704-0188), 1215 Jefferson Davis Highway, Suite 1204, Arlington, VA 22202-4302. Respondents should be aware that notwithstanding any other provision of law, no person shall be subject to any penalty for failing to comply with a collection of information if it does not display a currently valid OMB control number.
PLEASE DO NOT RETURN YOUR FORM TO THE ABOVE ADDRESS.

1. REPORT DATE (DD-MM-YYYY) 03/07/2018	2. REPORT TYPE Final	3. DATES COVERED (From - To) From 01/10/2012 to 29/03/2018
--	--------------------------------	--

4. TITLE AND SUBTITLE Advanced Photonics: Science, Technology and Applications	5a. CONTRACT NUMBER FA9550-12-1-0499
	5b. GRANT NUMBER
	5c. PROGRAM ELEMENT NUMBER

6. AUTHOR(S) Erich P. Ippen	5d. PROJECT NUMBER
	5e. TASK NUMBER
	5f. WORK UNIT NUMBER

7. PERFORMING ORGANIZATION NAME(S) AND ADDRESS(ES) Massachusetts Institute of Technology 77 Massachusetts Ave. Cambridge, MA 02139	8. PERFORMING ORGANIZATION REPORT NUMBER
--	---

9. SPONSORING/MONITORING AGENCY NAME(S) AND ADDRESS(ES) Air Force Office of Scientific Research Arlington, VA. 50488	10. SPONSOR/MONITOR'S ACRONYM(S) AFOSR
	11. SPONSOR/MONITOR'S REPORT NUMBER(S)

12. DISTRIBUTION/AVAILABILITY STATEMENT
A - Available for public release

13. SUPPLEMENTARY NOTES

14. ABSTRACT
Progress over the five year period of this contract has been reported in five previous annual reports. The topics covered in those reports are listed at the on page 2. The body of this report on pages 3-26 summarizes progress during the six month no-cost extension period 10/1/2017-3/29/2018. Topics include: sub-cycle control of soft X-ray HHG yield using two-color (f +3f) driver pulses, advances in nanostructured lightwave electronic devices, development of two-photon imaging technology for surgical imaging and optical biopsy, and nonlinear microscopy (NLM) for histological evaluation. The 120 publications produced under this contract over the period 2013-2018 are listed at the end on pages 27-36.

15. SUBJECT TERMS
Femtosecond lasers, nanophotonics, nonlinear optics, optical coherence tomography, nonlinear microscopy

16. SECURITY CLASSIFICATION OF:			17. LIMITATION OF ABSTRACT	18. NUMBER OF PAGES	19a. NAME OF RESPONSIBLE PERSON
a. REPORT	b. ABSTRACT	c. THIS PAGE			Erich P. Ippen
U	U	U	UU	36	19b. TELEPHONE NUMBER (Include area code) 617-253-8504

INSTRUCTIONS FOR COMPLETING SF 298

1. REPORT DATE. Full publication date, including day, month, if available. Must cite at least the year and be Year 2000 compliant, e.g. 30-06-1998; xx-06-1998; xx-xx-1998.

2. REPORT TYPE. State the type of report, such as final, technical, interim, memorandum, master's thesis, progress, quarterly, research, special, group study, etc.

3. DATE COVERED. Indicate the time during which the work was performed and the report was written, e.g., Jun 1997 - Jun 1998; 1-10 Jun 1996; May - Nov 1998; Nov 1998.

4. TITLE. Enter title and subtitle with volume number and part number, if applicable. On classified documents, enter the title classification in parentheses.

5a. CONTRACT NUMBER. Enter all contract numbers as they appear in the report, e.g. F33315-86-C-5169.

5b. GRANT NUMBER. Enter all grant numbers as they appear in the report. e.g. AFOSR-82-1234.

5c. PROGRAM ELEMENT NUMBER. Enter all program element numbers as they appear in the report, e.g. 61101A.

5e. TASK NUMBER. Enter all task numbers as they appear in the report, e.g. 05; RF0330201; T4112.

5f. WORK UNIT NUMBER. Enter all work unit numbers as they appear in the report, e.g. 001; AFAPL30480105.

6. AUTHOR(S). Enter name(s) of person(s) responsible for writing the report, performing the research, or credited with the content of the report. The form of entry is the last name, first name, middle initial, and additional qualifiers separated by commas, e.g. Smith, Richard, J, Jr.

7. PERFORMING ORGANIZATION NAME(S) AND ADDRESS(ES). Self-explanatory.

8. PERFORMING ORGANIZATION REPORT NUMBER. Enter all unique alphanumeric report numbers assigned by the performing organization, e.g. BRL-1234; AFWL-TR-85-4017-Vol-21-PT-2.

9. SPONSORING/MONITORING AGENCY NAME(S) AND ADDRESS(ES). Enter the name and address of the organization(s) financially responsible for and monitoring the work.

10. SPONSOR/MONITOR'S ACRONYM(S). Enter, if available, e.g. BRL, ARDEC, NADC.

11. SPONSOR/MONITOR'S REPORT NUMBER(S). Enter report number as assigned by the sponsoring/monitoring agency, if available, e.g. BRL-TR-829; -215.

12. DISTRIBUTION/AVAILABILITY STATEMENT. Use agency-mandated availability statements to indicate the public availability or distribution limitations of the report. If additional limitations/ restrictions or special markings are indicated, follow agency authorization procedures, e.g. RD/FRD, PROPIN, ITAR, etc. Include copyright information.

13. SUPPLEMENTARY NOTES. Enter information not included elsewhere such as: prepared in cooperation with; translation of; report supersedes; old edition number, etc.

14. ABSTRACT. A brief (approximately 200 words) factual summary of the most significant information.

15. SUBJECT TERMS. Key words or phrases identifying major concepts in the report.

16. SECURITY CLASSIFICATION. Enter security classification in accordance with security classification regulations, e.g. U, C, S, etc. If this form contains classified information, stamp classification level on the top and bottom of this page.

17. LIMITATION OF ABSTRACT. This block must be completed to assign a distribution limitation to the abstract. Enter UU (Unclassified Unlimited) or SAR (Same as Report). An entry in this block is necessary if the abstract is to be limited.

AFOSR Contract FA9550-12-1-0499

Final Report for the period 10/1/2012– 3/29/2018

Title: Advanced Photonics: Science, Technology and Applications

Investigators: Erich P. Ippen, James G. Fujimoto and Franz X. Kärtner

Institution: Massachusetts Institute of Technology

Summary

Progress over the five year period of this contract has been reported in five previous annual reports. The topics covered in those reports are listed at the on page 2.

The body of this report on pages 3-26 summarizes progress during the six month no-cost extension period 10/1/2017-3/29/2018. Topics include: Sub-cycle control of soft X-ray HHG yield using two-color ($\omega+3\omega$) driver pulses, Advances in nanostructured lightwave electronic devices, development of two-photon imaging technology for surgical imaging and optical biopsy and nonlinear microscopy (NLM) for histological evaluation.

A list of the 120 publication produced under this contract over the period 2013-2018 at the end on pages 27-36.

Topics Covered in Previous Annual Reports 2013-2017

2013

- (1) High-Harmonic Generation Close to the Multiphoton Ionization Regime
- (2) Electron Acceleration and Bunch Compression in THz Waveguides
- (3) Ultrahigh-Speed Endoscopic OCT) Using VCSEL Technology
- (4) High-Precision Ultralong-Range OCT
- (5) Swept-Source OCT Imaging of the Human Retina
- (6) Spectral Broadening in Anatase TiO₂ Waveguides at Telecom and Near-vis Wavelengths
- (7) Frequency Comb Based on a Narrowband Yb-fiber Oscillator
- (8) Sub-Femtosecond Timing Distribution Via a 1.2-km Polarization-Maintaining Fiber Link.

2014

- (1) High Power 2.2 μ m Laser and Soft X-ray HHG
- (2) Novel 3GHz Fiber Laser Systems
- (3) Nanostructure Photoemission for CEP Control
- (4) High Power THz Generation
- (5) THz-driven Electron Gun
- (6) THz-driven Linear Electron Acceleration
- (7) Nonlinear Microscopy for Cancer Diagnosis
- (8) Swept-source OCT for Long Range 3-D Imaging
- (9) Signal Processing for Motion Correction
- (10) Hand-held OCT System with MEMS Scanning

2015

- (1) Water-Window High-Harmonic Soft X-ray Source Using a kHz, Multi-mJ, 2.1- μ m OPCPA
- (2) Simulation of Water-Window High-Harmonic Generation in Neon
- (3) Probing Plasmonic Nanoparticles with Strong-field Photoemission
- (4) Optimization of Tilted-Pulse-Front Terahertz Generation
- (5) Multiphoton Microscopy for Surgical Pathology and Optical Biopsy
- (6) Next Generation OCT Using Advanced Photonics Technology
- (7) New Microscanning Imaging Devices
- (8) Real-Time Guidance of Ablation
- (9) Advanced Image Processing.

2016

- (1) High-Harmonic Generation in Solids Driven by Mid-IR pulses
- (2) Nanostructured, Lightwave Electronic Devices
- (3) Highly Efficient Broadband Terahertz Generation
- (4) Multiphoton Microscopy for Real-Time Pathology and Quantitative Optical Biopsy
- (5) Wide Field of View Multiphoton Microscopy System
- (6) Endoscopic Optical Coherence Tomography for Functional Imaging of the Gastrointestinal Tract.

2017

- (1) Mid-IR Sub-Cycle pulse synthesizer
- (2) Attosecond Pulse Characterization with a Volkov Transform Generalized Projection Algorithm
- (3) Phase-Sensitive, Field-Controlled Photoemission from Plasmonic Nanoantenna Arrays
- (4) THz Gun for Electron Acceleration
- (5) Long Range OCT
- (6) Endoscopic OCT
- (7) Multi-Photon Microscopy

1: Sub-cycle control of soft X-ray HHG yield using two-color ($\omega+3\omega$) driver pulses

The waveform of a driver pulse is critical for studying and controlling attosecond EUV and soft X-ray (SXR) HHG. The HHG yield is also highly dependent on the waveform with sub-cycle precision. Our collaborator C.D. Lin's group discovered by rigorous simulations that two-color mixed waveforms with ω and 3ω pulses are close to optimal for enhanced SXR HHG [Jin14]. Motivated by this work, we carried out a mid-IR two-color ($\omega+3\omega$, 2.1 μm and 700 nm)-driven HHG experiment for enhancement and sub-cycle control of HHG up to the SXR range [Kroh18]. In this study, we used Ar as the HHG medium because Ne is much harder to work with due to the high pressure required for good phase matching although the cutoff photon energy can reach up to the water-window region with Ne [Stein16]. In this section, we describe our experimental and theoretical study of HHG using waveform-controlled mid-IR pulses.

Experimental setup

The experimental setup of two-color HHG consists of four main parts: (i) a high-power OPCPA providing the fundamental pulses at 2.1 μm [Hong14], (ii) a dichroic Michelson-type interferometer to control the delay between the fundamental pulse and its third harmonic (700 nm), (iii) a custom-made HHG beamline equipped with a tailored gas cell and different diagnostic tools and (iv) detection units for the generated EUV and soft X-ray light, as illustrated as Fig. 1(a).

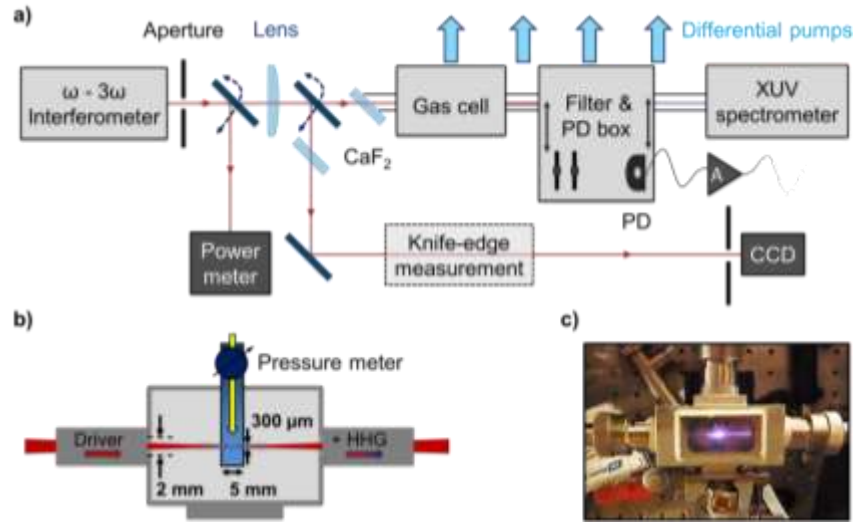


Figure 1: (a) Experimental layout of the HHG chamber and detection systems. A CaF₂ lens focuses the output of the Michelson type two-color interferometer into the gas cell (shown in detail in (b)) and HHG beamline. Different combinations of filters and EUV photo diodes (PD), connected to an electronic amplifier (A), or an EUV/SXR spectrometer can be used to characterize the generated high harmonics. (b) Layout of the custom designed gas cell of the HHG beamline. The driving field enters the cell from the left and interacts with the target gas (gas flow indicated by the yellow arrow) at adjustable pressure in the gas capillary (blue). (c) Picture of the Ar-filled gas cell driven by single color pulses from the OPCPA where the generated plasma is visible.

The 1.7 mJ, 26 fs, 2.1 μm pulses (ω pulses) from the 1 kHz OPCPA are frequency tripled in two subsequent BBO crystals via type-I SHG and type-II sum-frequency generation to 700 nm (3ω pulses). The ω and 3ω pulses then enter a Michelson-type interferometer equipped with a custom designed dichroic beam splitter for relative delay control. Residuals of any ω light in the 3ω arm are deflected by a thin ITO plate. The retro-reflector cube in the ω arm was mounted on a piezo motor with external controller which is used to scan the optical path difference for the pulses in steps of ~ 200 nm

(corresponding to temporal steps of 670 as). The rms timing jitter between the two pulses at fixed piezo position was determined to be ~ 397 as (corresponding to about 17 % of a single cycle of the 3ω pulse) after the interferometer over a duration of 4 s. The optical components of the interferometer together with the focusing optics before the HHG gas cell add dispersion to both ω and 3ω beams, resulting in slightly chirped pulses of approximately 37 fs and 26 fs duration, respectively.

After passing through an adjustable aperture, the output of the interferometer is focused using a CaF_2 lens ($f = 29$ cm) through a CaF_2 window into a custom designed gas cell with tunable Ar backing pressure. In the experiments for HHG, we use three different backing pressures of 375 mbar (optimal pressure for single-color driven HHG), 200 mbar and 143 mbar (lowest pressure yielding signal above noise floor). The beamline is equipped with a differential pumping stage leading to a chamber equipped with 500 nm thick Al- and Zr-filters used to block any residual pump light. In combination with two calibrated EUV photodiodes coated with Al and a Ti-C composition respectively (AXUV100Al and AXUV100Ti/C2, OptoDiode Corp.), the integrated high harmonic flux can be measured either in the range of $\sim 20 - 73$ eV or $85 - 205$ eV. A low-noise electric amplifier amplifies the photodiode (PD) signal. Harmonic spectra are measured with an EUV/SXR spectrometer. The two pulses are checked to overlap temporally via the fifth harmonic generation based on four-wave mixing ($\omega + \omega + 3\omega$) in air, while their spatial overlap at the focus was measured via the traveling knife-edge technique for the fundamental and with a CCD camera for the third harmonic. This way, the beam radius ($1/e^2$) is determined to be ~ 55 μm for the ω -beam and ~ 30 μm for the 3ω beam with the aperture set to a diameter of 7 mm.

The experiments were carried out under the following procedure: First, the single-color-driven HHG signal on the Al-coated PD was maximized using the adjustable iris and the position of the CaF_2 lens before the gas cell. The optimal aperture diameter was found to be about 7 mm which resulted in pulse energies of ~ 360 μJ (ω) and ~ 36 μJ (3ω), respectively. The corresponding peak intensities at the focus thus were $\sim 2.1 \times 10^{14}$ W/cm^2 and $\sim 9.6 \times 10^{13}$ W/cm^2 . The focus of the beams was set towards the rear end of the gas capillary and the interaction length was estimated to be approximately 3 mm. Before adding the 3ω beam, we collected the single-color driven HHG data both with the PD's and the spectrometer to later compare them with the two-color driven HHG data. To measure one full spectrum ranging from 35 to 220 eV we had to scan the CCD detection stack to four different positions on the Rowland circle of the EUV/SXR spectrometer. Once the single-color data was recorded, the third harmonic was added. Now we started scanning the relative delay. The piezo-motor in the interferometer was scanned while spectra or integrated yield were measured at each position. We used two filters, 0.5- μm -thick Al and Zr, to cover the whole spectral range of the generated high harmonics. The delay scans were performed with one filter first, before being repeated with the other. This allowed faster data acquisition, minimizing effects due to temperature drifts in our lab (scale of ~ 10 minutes). The downside of this procedure is that the two-color-driven HHG spectra obtained at different CCD positions are hard to be directly stitched together over the whole energy range of 30 to 220 eV, as a slight offset of relative delay could be introduced with the open-loop interferometer. This procedure, which is fully automated, was then repeated for each pressure.

Experimental results

HHG spectra have been measured with different relative phases over 4 different spectral ranges covering 35 – 210 eV. As an example, HHG spectra at 200 mbar Ar backing pressure are shown in Figs. 2(a) – (d). The recorded spectra exhibit a strong modulation of harmonic intensity with the two-color phase at a periodicity matching the period of the 3ω control pulse. We show the HHG spectra for three different relative phases within one modulation period ($\sim \pi/2$) for each spectral region. The dependence of the HHG spectral intensity on the relative phase is the strongest in the region below 60 eV. While significant enhancement compared to the single-color driven HHG level is observed at lower photon energies, this enhancement decreases towards higher photon energies. The same holds for the strength of the modulation imposed on the spectral intensity as a function of relative two-color phase. The modulation of harmonic yield is clearly visible in the integrated enhancement measured with the PDs as well, which is

shown in Fig. 3. The clear modulation with the optical cycle of the 3ω control field proves that the HHG process is manipulated at sub-cycle precision via changes in the relative delay (or relative phase near zero delay) of the two-color waveform.

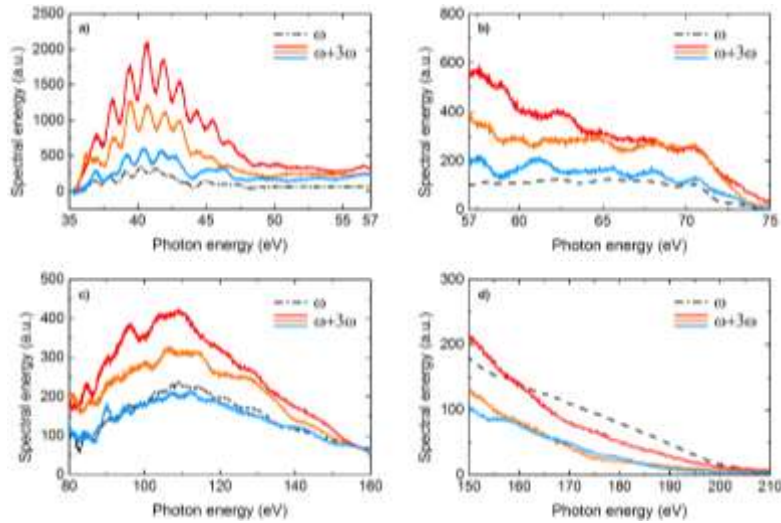


Figure 2: Selected two-color ($\omega+3\omega$) HHG spectra measured within one modulation period of the two-color waveform when scanning the two-color relative phase at a backing pressure of 200 mbar. The spectra were chosen as such to show the magnitude of modulation caused by scanning the $\omega-3\omega$ delay. For comparison the corresponding single-color (ω) driven spectrum is shown in black.

Figure 3 shows the tendency that the maximum enhancement and the magnitude of the modulation are lower at higher photon energies and higher pressure, which agrees with the observation from the HHG spectra. The plasma-induced phase mismatch has more dramatic impact on higher energetic HHG photons and higher pressure medium, as phase-slippage of the generated harmonics with respect to the driving waveform is larger. Additionally, the driving waveform itself suffers from dispersion which leads to an effective reshaping of the two-color waveform throughout its propagation through the interaction volume. This can be seen as an intrinsic scan of the two-color phase along the propagation, which effectively results in the detector averaging over several two-color phases. This averaging then reduces the magnitude of modulation.

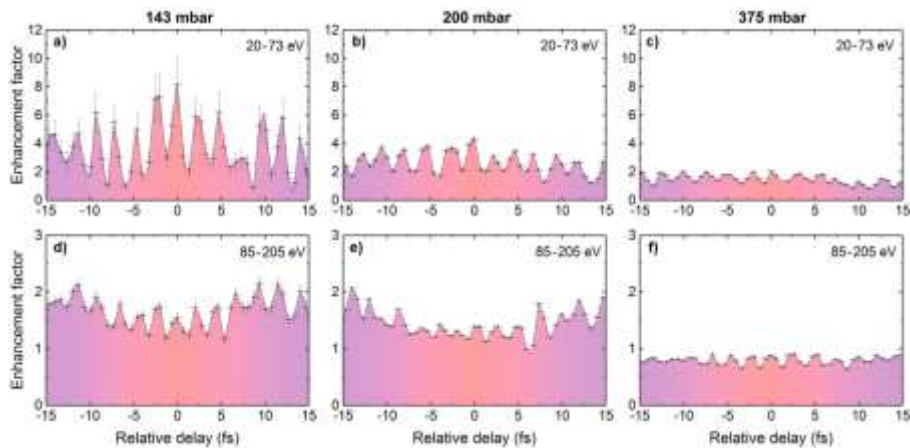


Figure 3: Integrated enhancement factors calculated from the measured EUV/SXR PD currents normalized by the single-color ω -driven signal for three different Ar backing pressures (noted at the top of each plot). The 0 fs position of the relative delay was chosen using the maximized FWM-based 5ω signal ($\omega+\omega+3\omega$) between ω and 3ω pulses in air. The black dashed line serves as a guide to the eye. The figures in the upper row show the enhancement factors integrated over photon energies between 20 – 73 eV, while the bottom row contains the data for 85 – 205 eV.

Although 375 mbar of backing pressure marks the optimal for the single-color driven case, we find the maximal observed enhancement by the added 3ω pulse to be the lowest at this pressure. Table 1 shows the maximal integrated enhancement factors recorded throughout the PD scans for each pressure, where the enhancement factors both measured between 20 – 73 eV and 85 – 205 eV drop with increasing Ar pressure. The drop of enhancement is observed to be more dramatic for the low energy, which reduce from a maximum of ~ 8 at 143 mbar to a factor of ~ 2 at 375 mbar. At higher photon energies, where the enhancement is less pronounced anyway, the value hardly drops between 143 mbar and 200 mbar and shows reduced photocurrent levels for all two-color delays at 375 mbar with a maximum reachable flux at only about 90 % of the single color level.

p (mbar)	Al-coated PD (20 – 73 eV)			TiC ₂ -coated PD (85 – 205 eV)		
	I _ω (pA)	I _{3ω} (pA)	Enhancement	I _ω (pA)	I _{3ω} (pA)	Enhancement
143	0.27	2.24	8.2	5.56	11.94	2.2
200	1.23	5.27	4.3	9.97	20.82	2.1
375	6.87	14.06	2.0	67.07	60.50	0.9

Table 1. Maximal enhancement factors of the integrated HHG yield between 20 – 73 eV measured with the EUV Al-coated PD and for 85 – 205 eV measured with the EUV TiC₂-coated PD for different pressures of Ar.

Comparison with simulations

We compare the experimental results to simulations using parameters as close as possible to experimental conditions. Since the high harmonics are coherently generated from all atoms in the gas medium involved in the strong-field interaction, a full description of experimentally observed HHG spectra consists of two parts: (i) the single-atom response, that is, the induced dipole by the driving laser field which can be obtained by solving the time-dependent Schrödinger equation (TDSE) or by an equivalent simpler model; and (ii) the macroscopic response, through solving the three-dimensional Maxwell’s wave equations for the fundamental laser and the high-harmonic fields, as described in detail in [Jin11]. In this work, the solution of the TDSE was replaced by using a quantitative rescattering (QRS) model [Le09].

We show the simulated HHG spectra generated by an unchirped ω pulse only, or by unchirped ω and 3ω pulses together, at three pressures: 76, 106, and 200 mbar in Figs. 4(a)–6(c). The relative phase between ω and 3ω pulses was scanned in the range between 0 and 2π . These spectra, smoothed according to the monochromator resolution, were compared with the experimental results obtained at the backing pressures of 143, 200, and 375 mbar, respectively. While it was impossible to directly measure the pressure in the interaction region during the experiment, we expect that it scales linearly with our backing pressure. To account for this discrepancy between our backing pressures and those of the interaction region, we used the measured and simulated single-color-driven HHG results. The simulations indicated that the optimal harmonic yields of single ω laser pulse occur at 200 mbar, while the experimentally observed optimal yields take place at a backing pressure of 375 mbar, resulting in a scaling factor of ≈ 0.53 . The simulated HHG spectra in Figs. 4(a)–4(c) clearly show that: (i) harmonic yields are sensitive to the relative phase between ω and 3ω pulses, which also explains the modulation of the harmonic yield as a function of relative delay seen in Fig. 3, (ii) for certain relative phases, the spectra can drop below the level of the single-color pumped case, (iii) higher enhancement is observed at lower photon energy, and (iv) a higher enhancement factor is observed at lower pressure, which are consistent with our experimental observations. However, the enhancement factor is consistently overestimated in comparison to our experimental results.

We also included the measured jitter in our interferometer (397 as corresponding to a phase jitter of 0.34π) by averaging over the two-color phase, which results in a significant reduction of the maximal observable spectral intensity and the contrast of the modulation with the two-color phase. The HHG

enhancement factors are shown in Fig. 4(d) for a gas pressure of 200 mbar (corresponding to 375 mbar backing pressure), at which we obtained the highest overall signal in the experiment. With the spectrometer resolution and the two-color phase jitter applied, a better overall qualitative agreement with the experiment can be achieved. The enhancement factor drops to a value close to unity for a broad range of two-color phases for photon energies above 100 eV. This describes the overall trend well, with the enhancement still being predicted slightly higher in the simulations than in the experiment (factor of ≈ 10 around 110 eV, factor of ≈ 5 around 140 eV for 375 mbar backing pressure). Especially for photon energies above 100 eV, where the structure of the Cooper minimum does not affect the macroscopic HHG spectra, Fig. 4(d) shows more realistic enhancement factors close to the ones we can observe from experiments.

We also studied other effects changing the harmonic yield. A separate simulation confirms that the chirp of the experimental waveforms play no significant role. As slight chirp does not greatly change the instantaneous frequency in the center part of the pulse, which is where most HHG occurs, it does not significantly affect the two-color-driven HHG. Other experimental parameters that were modeled in an idealized way in the simulations, such as the exact distribution of the gas medium or the actual quality of the wave fronts at focus, lead to the simulations predicting slightly higher enhancement factors than the experimental observations. In addition, it is still hard to predict the exact shape of the Cooper minimum computationally, which is a possible reason of overestimation for photon energies nearby.

Based on our findings, we expect the enhancement to be further improved by a factor of ≈ 2 at 375 mbar backing pressure, if the open-loop interferometer in the experiment would be actively stabilized to a realistic jitter of ≈ 10 as. The yield at lower pressures should benefit from a lower jitter even more, as the depth of modulation of the yield with the two-color phase is more significant at lower pressure. As already suggested by the experimental findings, once tuned to the optimal two-color phase, the pressure could then be optimized separately for this specific waveform. Therefore, global optimization would make the two-color approach more useful towards higher enhancement factors in the SXR range.

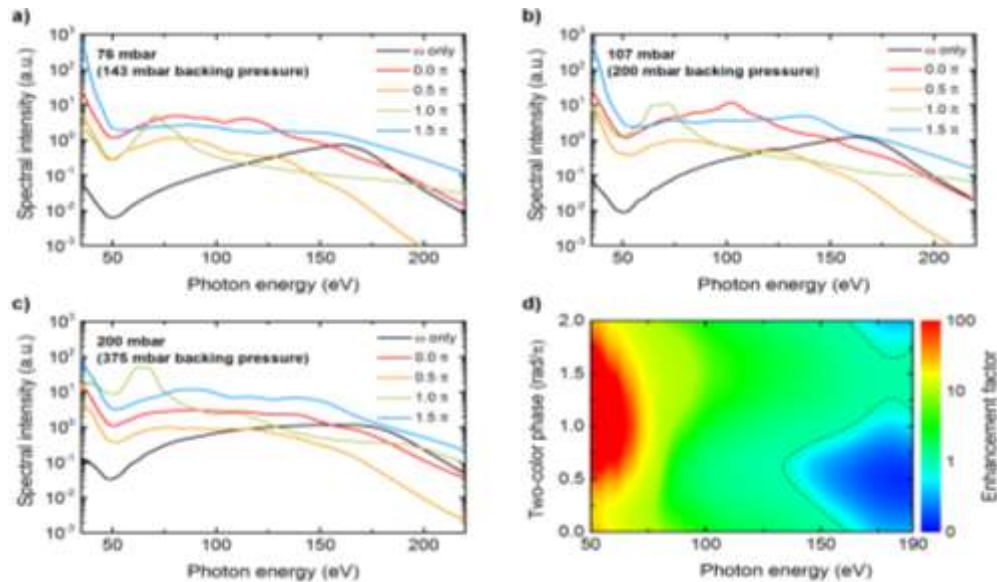


Figure 4: Simulated HHG spectra depending on pressure and two-color phase. Experimental backing pressures (given in brackets) are specified along with the corresponding pressure at the interaction region. (a) – (c) show the two-color driven HHG spectra and the single-color driven spectrum (black). The simulated HHG enhancement factors for 200 mbar (backing pressure of 375 mbar), taking the spectrometer resolution and experimental jitter (≈ 400 as) in the two-color phase (via smoothing along the energy and phase-axis using Gaussians of the corresponding widths) into account, are shown in (d).

Our work suggests that for high-pressure gas HHG setups (e.g. using helium) [Popmintchev11], which need multiple differential pumping stages to maintain the vacuum level for the detection, two-color driving schemes open the perspective of reducing the target gas pressure while maintaining the flux-level of the high harmonics. For further extension of the enhancement to higher photon energies considerable effort will have to be put into the stabilization of the driving waveform first, which is also a problem current optical synthesizer are facing. Future work may thus be dedicated to this problem and focus on finding a global macroscopic optimum for each driving waveform. At stabilized conditions a two-color approach using even longer driving wavelengths in the mid-IR is expected to boost the spectral content in the plateau region of the HHG spectrum – possibly up to the water window regions.

References

- [Henke93] B. L. Henke, E. M. Gullikson, and J. C. Davis, “X-ray interactions: Photoabsorption, scattering, transmission, and reflection at $E = 50\text{-}30,000$ eV, $Z = 1\text{-}92$,” *Atomic Data and Nuclear Data Tables* **54** (2): 181 – 342 (1993).
- [Hong14] Kyung-Han Hong, Chien-Jen Lai, Jonathas Siqueira, Peter Krogen, Jeffrey Moses, Chun-Lin Chang, Gregory J. Stein, Luis E. Zapata, and Franz X. Kärtner, “Multi-mJ, kHz, $2.1\text{-}\mu\text{m}$ optical parametric chirped pulse amplifier and high-flux soft X-ray high-harmonic generation,” *Opt. Lett.* **39**, 3145-3148 (2014).
- [Jin14] C. Jin, G. Wang, H. Wei, A.-T. Le, and C. D. Lin, “Waveforms for optimal sub-keV high-order harmonics with synthesized two- or three-colour laser fields.” *Nature Communications* **5**, 4003 (2014).
- [Jin11] C. Jin, A.-T. Le, and C. D. Lin, “Medium propagation effects in high-order harmonic generation of Ar and N_2 ,” *Phys. Rev. A* **83**, 023411 (2011).
- [Kroh18] T. Kroh, C. Jin, P. Krogen, A.-L. Calendron, P. D. Keathley, J. P. Siqueira, H. Liang, E. L. Falcão-Filho, C. D. Lin, F. X. Kärtner and K.-H. Hong, “Enhanced high-harmonic generation up to the soft X-ray range driven by mid-IR pulses mixed with their third harmonic,” *Optics Express, in press* (2018).
- [Le09] A.-T. Le, R. R. Lucchese, S. Tonzani, T. Morishita, and C. D. Lin, “Quantitative rescattering theory for high-order harmonic generation from molecules,” *Phys. Rev. A* **80**, 013401 (2009).
- [Popmintchev11] T. Popmintchev, M.-C. Chen, D. Popmintchev, P. Arpin, S. Brown, S. Ališauskas, G. Andriukaitis, T. Balčiunas, O. D. Mücke, A. Pugzlys, A. Baltuška, B. Shim, S. E. Schrauth, A. Gaeta, C. Hernández-García, L. Plaja, A. Becker, A. Jaron-Becker, M. M. Murnane, and H. C. Kapteyn, “Bright coherent ultrahigh harmonics in the keV x-ray regime from mid-infrared femtosecond lasers,” *Science* **336**, 1287 (2012).
- [Stein16] G. J. Stein, P. D. Keathley, P. Krogen, H. Liang, J. P. Siqueira, C.-L. Chang, C.-J. Lai, K.-H. Hong, G. M. Laurent, and F. X. Kärtner, “Water-window soft X-ray high-harmonic generation up to nitrogen K-edge driven by a kHz, $2.1\ \mu\text{m}$ OPCPA source,” *J. Phys. B* **49**, 155601 (2016).

2: Advances in Nanostructured, Lightwave Electronic Devices

During this reporting period, we have made important progress in the development of nanoantenna arrays for carrier-envelope-phase (CEP) detection. These results have already culminated in three conference papers (Keathley 2018, Putnam 2018, and Chia 2018), and are currently being prepared for publication. Here we highlight three key results obtained in this reporting period: (1) the observation of antiresonant-like features in CEP-sensitive photocurrent as a function of incident laser intensity; (2) the first experimental demonstration of electrically connected nanoantenna arrays for improved optical sensitivity, high-speed performance, and noise reduction; and (3) demonstration that our nanoantenna CEP detectors are already operating close to the shot-noise limit. We discuss these three results in more detail below.

Antiresonant-Like Behavior in CEP-Sensitive Photocurrent

The electric field of ultrafast optical pulses can control electrical currents around nanoscale vacuum electronic structures at frequencies exceeding **100 THz** (Krüger 2011, Piglosiewicz 2014, Rybka 2016, Putnam 2017). Such extreme electrical control requires optical-field emission, *i.e.* the emission of sub-optical-cycle bursts of electrons via optical-field-driven tunneling. A hallmark of optical-field emission is sensitivity of the total emitted current to the carrier-envelope phase (CEP) of the driving optical pulse. Such CEP-sensitive photocurrent has been observed in the emitted electron spectra from isolated nanotips (Krüger 2011, Piglosiewicz 2014), and more recently in total current yields from nanoscale structures (Rybka 2016, Putnam 2017). Here, we present a study of optical-field-controlled, CEP-sensitive photoemission from nanoantennas performed under varying optical intensity. We observed antiresonant-like behavior in the photocurrent's CEP response where at a critical intensity the CEP-sensitive

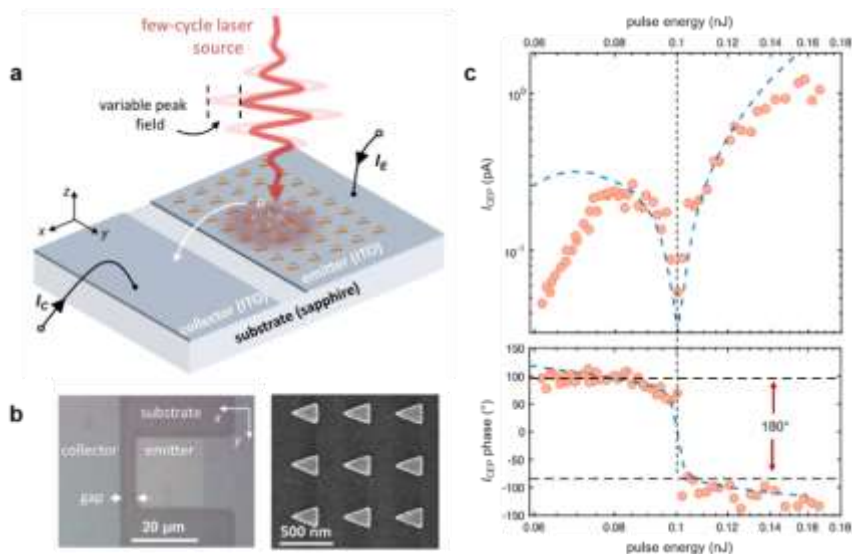


Fig. 1: **a.** Experimental setup. Few-cycle laser pulses of tunable pulse energy and peak field produce photoemission currents from gold nanotriangles, and these currents are pulled from an emitter electrode to a collector (emitter and collector currents are labeled I_E and I_C respectively). **b.** Optical and electron microscope images of a nanotriangle emitter array. **c.** Measured CEP-sensitive current (I_{CEP}) versus the

photocurrent exhibited a significant dip in magnitude as well as a dramatic **180°** shift in phase. Using a quasi-static tunneling model, we attribute this behavior to competition between sub-optical-cycle bursts of charge.

Our experimental approach followed earlier work (Putnam 2017) and is illustrated in Fig. 1a. Arrays of gold nanotriangles were fabricated onto a transparent and conducting indium tin oxide (ITO) film on a sapphire substrate. An ITO collector electrode was located across a $\approx 5 \mu\text{m}$ gap from the nanotriangle

emitter array; micrographs are provided in Fig. 1b. The nanotriangles were illuminated with tightly-focused ($\approx 5 \mu\text{m}$ beam diameter) few-cycle laser pulses (≈ 10 fs duration at a center wavelength of 1177 nm corresponding to ≈ 2.5 cycles). When excited by few-cycle laser pulses, the nanotriangles' localized surface plasmon resonance (LSPR) and sharp features result in enhanced local optical fields. Our measurements indicate a field enhancement of ≈ 32 , which agrees well with prior work under identical illumination conditions (Putnam 2017). With incident pulse energies ranging between 50-160 pJ, we have enhanced peak fields of 18-32 V/nm (*i.e.* Keldysh parameters of 0.67-0.38). Such strong-fields lead to large photoemission currents (tens of nA). Additionally, with such high fields the photoemission occurs in the strong-field regime where the emission process resembles quasi-static optical tunneling, and the emitted current becomes CEP-sensitive.

We stabilized the CEP of our few-cycle laser source by locking the carrier-envelope offset frequency, f_{CEO} , to a stable 100 Hz reference. We measured the CEP-sensitive component of the emission current, *i.e.* the component of the current at f_{CEO} , via lock-in detection in a 125 mHz bandwidth. In the top panel of Fig. 1c, the CEP-sensitive current, denoted I_{CEP} , is displayed versus driving pulse energy; in the bottom panel the phase of I_{CEP} relative to the f_{CEO} reference is also plotted. We see that I_{CEP} displays antiresonant-like behavior: near 100 pJ pulse energies the magnitude of I_{CEP} abruptly dips, and the phase of I_{CEP} swings by $\approx 180^\circ$. To understand the origins of this behavior, we used a quasi-static tunneling model. We started with \cos^2 -shaped model pulses (10 fs duration and 1177 nm center wavelength) and then filtered these pulses with the experimentally-characterized transfer function of the plasmonic nanoantennas (the particles were modeled as resonators). Next, we calculated the quasi-static Fowler-Nordheim (FN) tunneling currents driven by these filtered pulses with varying CEP's. After integrating the current over each pulse in both space and time, we then calculated total emitted charge versus CEP

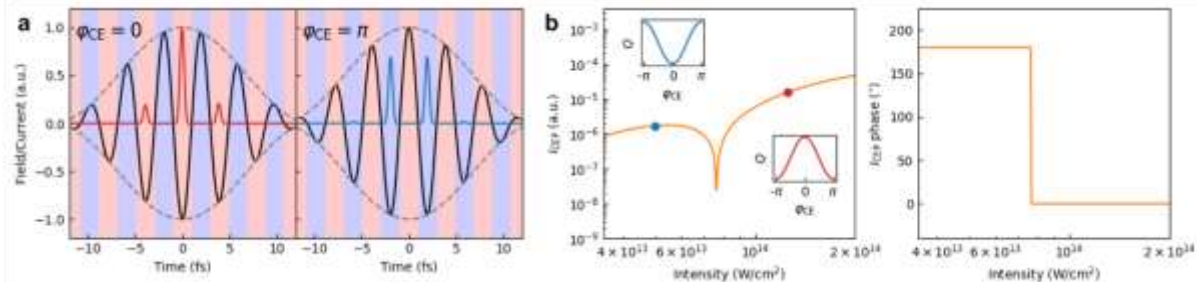


Fig. 2: **a.** Fowler-Nordheim tunneling emission (red and blue curves) from a \cos^2 -shaped model pulse (black curve) with $\varphi_{\text{CEP}} = 0$ (left panel) and $\varphi_{\text{CEP}} = \pi$ (right panel). Even half-cycles are shaded red, and odd blue. Note that here we define $\varphi_{\text{CEP}} = 0$ to correspond to a negative peak field. **b.** The CEP-sensitive current (left) and relative phase (right) for a \cos^2 -shaped model pulse with 10 fs duration exciting a gold

and estimated I_{CEP} . We repeated this process for pulses of varying energy to build a simple model of our experiment. The model results are plotted in Fig. 1c (blue, dashed curve) and show excellent agreement with the experimental data.

To provide further insight into the antiresonant-like behavior, we removed the plasmonic filtering from our quasi-static model and repeated I_{CEP} calculations using a 10 fs duration \cos^2 pulse centered at 1177 nm (see waveforms in Fig. 2a). In Fig. 2a, the current profiles from our quasi-static model are shown for two possible CEP phases, $\varphi_{\text{CEP}} = 0$ and $\varphi_{\text{CEP}} = \pi$ (red and blue curves respectively). For analysis purposes, half-cycle regions are highlighted (red and blue regions). Note that the even half-cycles (red regions) exhibit peak yield at or near $\varphi_{\text{CEP}} = 0$, and the odd half-cycles (blue regions) at or near $\varphi_{\text{CEP}} = \pi$. The magnitude and phase of the calculated I_{CEP} is plotted in Fig. 2b as a function of peak optical intensity at the emitter surface. We found that the cause of the antiresonant-like feature in I_{CEP} shown in Fig. 2b is a transition from the photoemission being dominated by odd half-cycle contributions to being dominated by even half-cycle contributions. This is evidenced in the response of total charge

yield as a function of φ_{CEP} before and after the dip in I_{CEP} . For example, at a peak intensity of 50 TW/cm^2 charge emission, Q , peaks at $\varphi_{\text{CEP}} = \pm\pi$ (blue dot and top inset in Fig. 2b), and at 125 TW/cm^2 it peaks at $\varphi_{\text{CEP}} = 0$ (red dot and bottom inset in Fig. 2b). At a critical intensity near 80 TW/cm^2 , the even half-cycle contributions match those of the odd half-cycles, resulting in a sharp decrease in I_{CEP} as the two are separated in phase by 180° . As the critical intensity point represents the switch between even and odd half-cycle dominance, the phase of I_{CEP} also experiences a sudden 180° swing at this point (right panel of Fig. 2b).

In summary, we measured CEP-sensitive photoemission currents from plasmonic nanoantennas driven by few-cycle laser pulses with optical pulse energies ranging between 50-160 pJ. We observed antiresonant-like behavior in the CEP-sensitive current and attribute this behavior to competing emission from different optical half-cycles of the driving laser pulses. While we observed this behavior in total current yields from nanostructured devices, we emphasize that this antiresonant-like behavior in strong-field photoemission is general in nature and should be observable using other systems, such as atoms or molecules. This work has been accepted to both the 2018 International Conference on Ultrafast Phenomena (Keathley 2018) and the 2018 Conference on Lasers and Electro-Optics (CLEO) (Putnam 2018).

Electrically Connected Nanoantenna Arrays and their Fundamental Noise Limitations

In previous work (Putnam 2017) we showed that optical-field emission from sub-wavelength nanoantennas can be used to detect the CEP of few-cycle optical pulses. CEP detection is necessary for the stabilization of optical frequency combs, as well as for strong-field nonlinear optics and attosecond science applications that require field-level control of ultrafast optical pulses. In this work we demonstrate the detection of CEP-sensitive photocurrents in a parallelized array of electrically connected bowtie nanoantennas (Prangma 2012, Zimmerman 2018). Investigating the background noise of the photocurrent, we show that we achieve performance close to the shot-noise limit from these electrically connected nanoantenna arrays. With a higher pulse energy laser source, similar, compact nanoantenna-based optoelectronic devices should allow for direct CEP monitoring and tagging (Wittmann 2009).

Our electrically connected nanoantenna arrays were fabricated on a glass (BK7) substrate, and consist of 20-nm-thick, gold bowtie antennas having a plasmonic resonance near 1200 nm. The bowties have average gap widths of $\approx 20 \text{ nm}$ across a $200 \mu\text{m}^2$ area containing a total of 288 bowties (see Fig. 1a). We illuminated the arrays with an optical pulse train having a repetition rate of 78 MHz, an average pulse duration of ≈ 2.5 cycles at a center wavelength of 1177 nm ($\approx 10 \text{ fs}$ FWHM), a maximum pulse energy of $\approx 190 \text{ pJ}$, and a spot size of $\approx 2.25 \mu\text{m} \times 4.1 \mu\text{m}$ FWHM (our beam spot was smaller than the entire nanoemitter array). The carrier-envelope offset frequency, f_{CEO} , of the pulses was locked to a reference

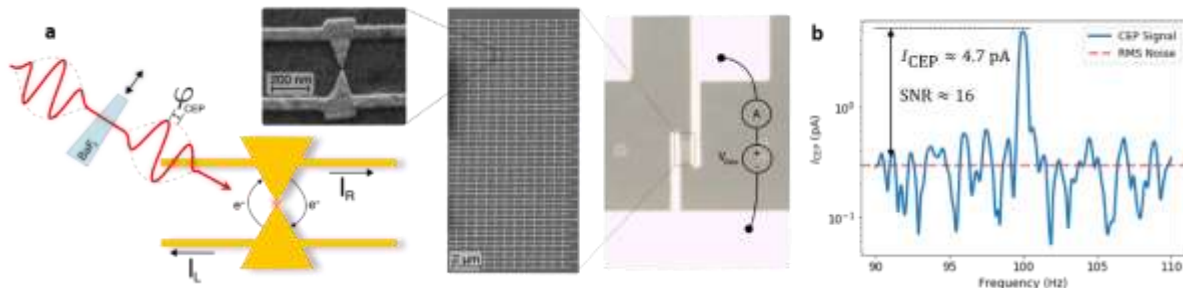


Fig. 1 (a) Schematic showing optical pulse excitation of a unit-cell of the nanoantenna array. An absolute CEP-phase offset, φ_{CEP} , is introduced by inserting a BaF_2 wedge. Wires carry a right-going current, I_{R} , from the top emitters to the right contact, and a left-going current, I_{L} , from the bottom emitters to the left contact. The images show the device at three different scales (from left to right): a micrograph of a single bowtie antenna, a micrograph of the entire nanoantenna array, and a microscope image of the left/right contacts that connect the

using an f - $2f$ interferometer, and the nanoantennas' photocurrent was amplified using a trans-impedance amplifier before detection.

The maximum observed CEP-sensitive photocurrent, I_{CEP} , was ≈ 5 pA (see Fig. 1b). While not every region of the emitter array exhibited such high performance, scanning our beam across the array we measured I_{CEP} values ranging from hundreds of fA to several pA. To ensure that the observed signal indeed arises from CEP-sensitive photoemission, we moved a BaF₂ wedge (see Fig. 1a) through the beam while monitoring the phase of the f_{CEO} signal. The wedge was stepped forward by 2.5 mm every 20 s. We measured an average phase shift of 58.6°/step which matches well to the predicted value of 58.3°/step (see Fig. 2a). Given that there were roughly 22-23 emitters (note that each bowtie antenna contains two emitters) within the FWHM beam spot area, and assuming these emitters dominate photoemission, we calculate an average CEP-sensitive emission of ≈ 0.21 pA/emitter. This is roughly a $4 \times$ increase in CEP-sensitive emission per-emitter compared to single-triangle emitters when operated under nearly identical conditions (Putnam 2017). We attribute the increase in CEP-sensitive current to both increased optical field enhancement and improved electron transport across the nm-scale gap. The CEP-sensitive current also scales favorably with recent results from (Rybka 2016) where roughly 0.2-0.25 pA/emitter was observed when using only a single bowtie pair (note that this result was for a 1.6-cycle pulse).

For an ideal bowtie nanoantenna, there should be no net DC-offset current (*i.e.* net background current insensitive to the CEP). Due to nonidealities, DC-offset current was observed, but was found to be controllable by tuning the bias voltage, V_{bias} (defined in Fig. 1a), as shown in plot of DC-offset current as a function of V_{bias} in Fig. 2b. While the zero-point of the DC-offset current was found at $V_{\text{bias}} \approx -0.5$ V, we repeated this measurement at various spots on the nanoantenna array, finding zero-points at V_{bias}

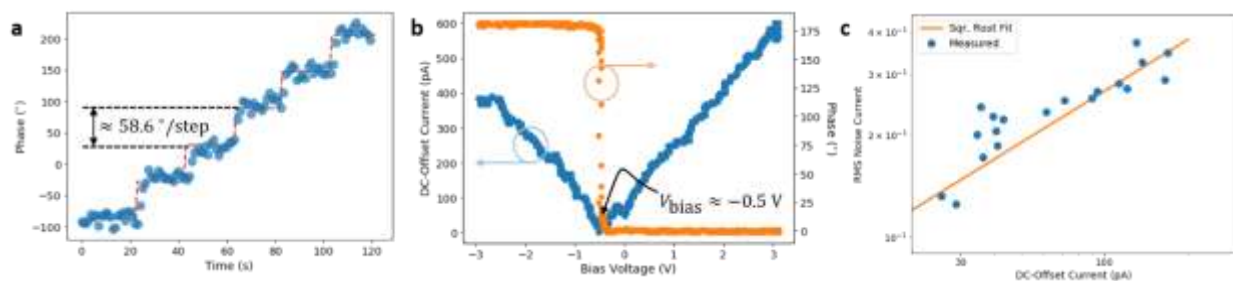


Fig. 2 (a) Phase of CEP-sensitive signal as a function of time. A BaF₂ wedge was inserted by 2.5 mm every 20 s leading to an average phase shift of $\approx 58.6^\circ$ per insertion. (b) DC-offset current versus V_{bias} . DC-offset current was measured by chopping the beam and using lock-in detection with the CEP unlocked. The blue curve shows the magnitude of the current, and the orange the phase (relative to the chopper frequency). The

values ranging from -1 V to $+1$ V. In all cases the noise floor was insensitive to V_{bias} , and was of similar magnitude to the noise-floor observed using arrays of single-triangle emitters (see devices in [Putnam 2017]), likely ruling out low-frequency intensity fluctuations of the optical pulse energy as the dominant noise source. However, the noise floor was sensitive to the optical illumination and/or current emission as there was a ≈ 20 dB drop in the noise floor upon blocking the beam.

To investigate the character of the noise, we set $V_{\text{bias}} = 3$ V for maximum DC-offset current, which we assume to be directly proportional to the total average emitted current from all emitters, I_{avg} . We then examined the noise floor level relative to the DC-offset current while changing the incident pulse energy. These results are shown in Fig. 2c. The noise-floor level fits well to a square-root dependence on the DC-offset current, a hallmark of shot-noise. Given that shot-noise should scale as $\sqrt{2qI_{\text{avg}}\Delta f}$, where q is the electron charge, and Δf the resolution bandwidth of the measurement, we find the measured noise floor would correspond to $I_{\text{avg}} \approx 65$ nA at 190 pJ, which translates to ≈ 3 nA/emitter. This is a $3 \times$ increase in

I_{avg} relative to our prior observation of ≈ 1 nA/emitter using an array of single-triangles (Putnam 2017), which compares favorably to the corresponding $4 \times$ increase in I_{CEP} per-emitter. We find these results to be convincing evidence that the devices were operated close to their shot-noise-limited signal-to-noise ratio. This further necessitates arrays of plasmonic emitters to boost the detection CEP-sensitive signals as there are only two ways to overcome such noise: (1) increase the CEP-sensitivity ($I_{\text{CEP}}/I_{\text{avg}}$), and/or (2) increase the overall collected signal.

In summary, we have demonstrated the feasibility of parallelizing large arrays of electrically connected bowtie emitters for improved CEP detection, pushing lightwave electronics from the realm of physics into that of high-speed optoelectronic device engineering. Higher currents were achieved relative to arrays of single-triangles due to increased plasmonic enhancement and improved electron collection. Furthermore, the few-nm gaps allowed for electron transport and collection without the need for conducting substrates or large bias voltages (Putnam 2017), and improve the fundamental limits on the devices operating frequency. With increased laser pulse energies and array sizes, we predict that such nanoantenna emitters will be an attractive, on-chip alternative for CEP monitoring and tagging. These results are currently being compiled for publication.

References

- (Chia 2018) S.-H. Chia *et al.*, *XXI International Conference on Ultrafast Phenomena* (2018).
- (Keathley 2018) P. Keathley *et al.*, *XXI International Conference on Ultrafast Phenomena* (2018)
- (Krüger 2011) M. Krüger, M. Schenk, and P. Hommelhoff, *Nature* **475**, 78 (2011).
- (Piglosiewicz 2014) B. Piglosiewicz, *et al.*, *Nature Photonics* **8**, 37 (2014).
- (Prangma 2012) J. C. Prangma *et al.*, *Nano Lett.*, **12**, 3915 (2012).
- (Putnam 2017) W. P. Putnam *et al.*, *Nat. Physics*, **13**, 335 (2017).
- (Putnam 2018) W.P. Putnam *et al.*, *2018 Conference on Lasers and Electro-Optics* (2018).
- (Rybka 2016) T. Rybka *et al.*, *Nat. Photonics*, **10**, 667 (2016).
- (Wittmann 2009) T. Wittmann *et al.*, *Nat. Physics*, **5**, 357 (2009).
- (Zimmerman 2018) D. T. Zimmerman *et al.*, *Journal of Applied Physics*, vol. **123**, 063101 (2018).

3: Development of Two-Photon Imaging Technology for Surgical Imaging and Optical Biopsy Introduction to Nonlinear Microscopy (NLM)

Multiphoton and nonlinear microscopies have had a revolutionary impact on fundamental scientific research and biological imaging in fields ranging from cell biology to neurosciences (1, 2). NLM can achieve cellular resolution and high contrast axial sectioning in thick tissue specimens by point scanning femtosecond pulse duration near-infrared light across tissue. However, NLM can also provide molecular specific contrast using both extrinsic probes and intrinsic fluorescence, enabling it to visualize many of the same biochemical markers that are the hallmarks of pathology in conventional histological examination. The excellent resolution and molecular contrast available with NLM are particularly well-suited for visualizing subcellular-resolution features, such as nuclear size and shape, and morphological changes in tumor extracellular matrix and stroma, such as reorganization of collagen, which are important hallmarks of neoplasia (3-6).

A major advantage of NLM is the ability to use fluorescent probes that rapidly target specific cellular agents, including DNA, specific proteins and cellular receptors. By carefully choosing contrast agents, NLM images can be generated from unfixed tissue that closely approximate more familiar microscopy techniques, such as the use of DNA-specific dyes and transmission wide-field microscopy in conventional clinical histopathology, but without the lengthy (20+ hour) processing. This concept is illustrated in Figure 1, where an intact, unprocessed human breast tissue specimen has been stained analogously to conventional H&E histology and then optically sectioned using NLM. Consequently, NLM has the potential to enable real-time evaluation of surgical specimen pathology in an intraoperative setting while retaining familiar markers of pathology from conventional histology.



Figure 1. Virtual 3D H&E histopathology performed using nonlinear microscopy of freshly excised, unfixed normal human breast tissue showing collagen fibers (red through pink) and cell nuclei (purple).

Development of Portable, High-speed Nonlinear Microscopy for Surgical Evaluation Using GPU Acceleration

Existing NLM apparatus is too large in size and produces images too slowly for medical applications. To enable clinical translation, we have miniaturized NLM technology to produce a portable, inverted NLM system including microscope and femtosecond laser, operating on a 2.5 by 3 foot cart suitable for operation in a clinic. The new system (Figure 2) incorporates lower magnification, wide field of view imaging optics which enable variable 5x (3.4 mm x 3.4 mm), 10x (2 mm x 2 mm FOV), 20x (1 mm x 1 mm) and 40x (0.5 mm x 0.5 mm) magnification imaging similar to a conventional histology microscope(7). At lowest magnification, the system enables area imaging rates of 145 mm²/s, dramatically faster than existing NLM technology. To enable real-time, high frame rate imaging of samples, we have developed and implemented a physically-realistic light absorption model for virtual H&E rendering on a graphics processing unit (GPU)(8). The use of GPU rendering enables very low latency, high quality virtual H&E rendering of images at very high pixel rates (1 MP/image at 16 frames per second). Finally, the inverted geometry enables rapidly placing multiple large samples onto a common imaging plate, facilitating rapid evaluation of multiple and irregularly sized surgical specimens.

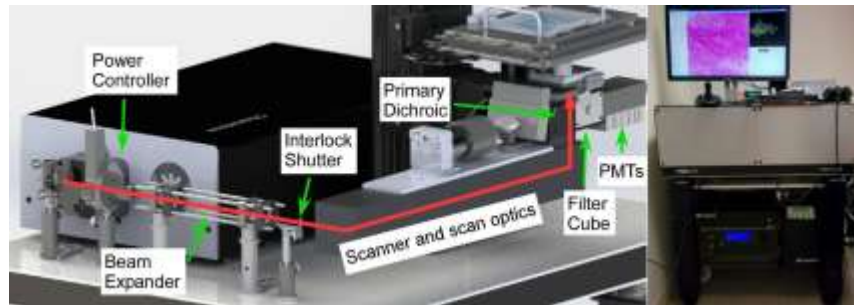


Figure 2. Portable NLM system deployed at BIDMC in Boston (left). The system incorporates a tunable femtosecond laser, inverted laser scanning optics, pneumatic vibration isolation, a large area translation stage (right image, 6 cm by 9 cm area) and a white light imaging for sample orientation all enclosed in a 2.5x3 foot light-tight enclosure that can be used in a clinic.

The portable NLM system further incorporates a software user interface that replicates the appearance of a conventional histology microscope (Figure 3). In addition to VHE rendering for ease of interpretation, a “focus” knob is used for Z-depth actuation, while a keypad enables rapid (<1 second) change of magnification. Finally, the specimen holder (Figure 4) is monitored at video rate using optical position encoders, and the current NLM imaging position is rendered over a white light image of the tissue specimens, enabling the operator to rapidly (seconds) survey the entire surface of the tissue specimen for the presence of surgical marking inks and then direct imaging to critical locations. Because of the efficient workflow, large (50 cm²) can be evaluated in minutes.



Figure 3. Software user interface and controls used to image freshly excised, inked bread loafed breast specimens. The VHE display shows a terminal ductal lobule unit (TDLU) imaged at 20x magnification, while the white light microscopy shows a gross image of the tissue with the current imaging location adjacent to a simulated margin painted in ink. The user can rapidly (< 1 second) adjust the magnification using a control pad, while a joystick and digital focus knob are used for X/Y and Z control, respectively. An LED indicator shows the laser interlock status, enabling the operator to see when the specimen is loaded and the laser armed.



Figure 4. Specimen tray. Render of the design files used for the interchangeable specimen tray (left) and the system as fabricated and loaded with 6 inked, bread loaf sectioned breast specimens (right). The tray incorporates a lid with fill port as well as inset dividers that can be used to separate multiple small specimens.

Development of Computational Methods for Stitching NLM Videos into Seamless Mosaics

Conventional histology generates a permanent record of each histological image in the form of a glass slide that can be achieved for future review. In analogy with conventional glass slides, we have developed hardware and software approaches for fusing video frames from live (operator-controlled) NLM evaluation sessions into seamless mosaic images that simulate a whole slide image and can be evaluated analogously to conventional slides. Figure 5 demonstrates our approach, which records the motion of the specimen using optical encoders as well as the location of the laser of scanning on the specimen synchronously at every 125 microseconds, or approximately every 2048 pixels. Because the dwell time of an NLM pixel is measured in microseconds, individual pixels have no motion artifacts even when translated at centimeters per second. By measuring the position of the laser and the displacement of the specimen at highspeed, individual pixels can be assigned to their true position on the specimen even if the operator translates the imaging location rapidly. This process effectively removes the effect of motion from the images, generating a complete record of all tissue evaluated during a surgical procedure.

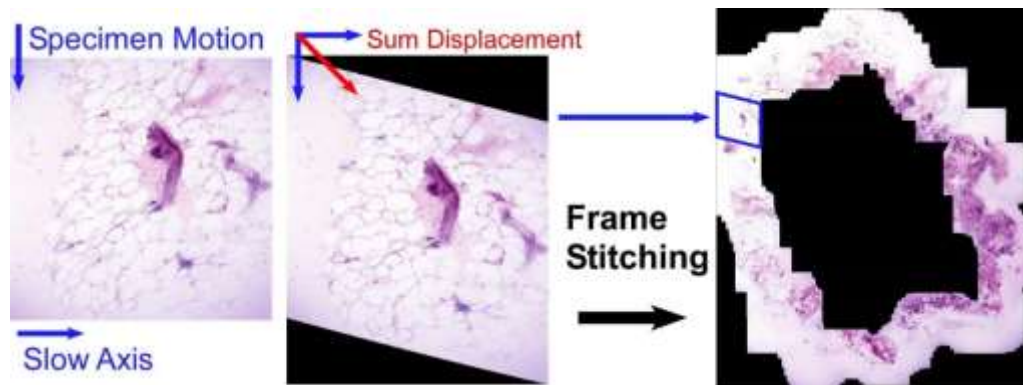


Figure 5. Dewarping and stitching of live data to generate mosaics. By synchronously reading out position data with each fast axis cycle, the true geometric position of all pixels in each image can be calculated and the resulting frames stitched into an undistorted mosaic.

We further deployed this technology to rapidly evaluate inked breast tissue during simulated surgical procedures. Figure 6 shows a simulated positive breast surgical margin created by dissecting a large whole breast resection such that a region of tumor and adjacent normal tissue were included on the same specimen. The specimen has yellow ink applied to the positive margin, and green and orange ink on the negative margins. The operator evaluated all three margins by rapidly panning between them using the white light image for orientation and to locate the precise areas of surgical marking ink. The simulated evaluation was repeated twice, once using 10x magnification only and again using variable magnification using both 5x and 10x objectives. Both procedures were recorded and then computationally stitched into a whole slide images. Remarkably, although the specimen is several square centimeters, using variable magnification imaging, the operator was able to locate the positive margin while excluding all negative margins in less than 30 seconds, as compared to nearly 20 minutes required using conventional frozen section intraoperative histology. These results demonstrate that advanced NLM imaging technology can be used to image surgical specimens dramatically faster than currently accepted methods, potentially enabling more efficient surgical management of cancer.

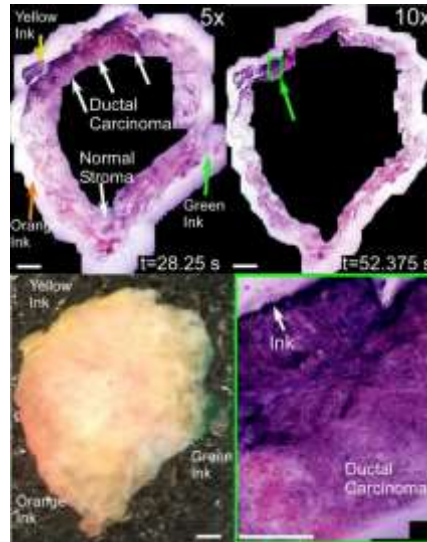


Figure 6. Stitching of video frames into mosaics. 5x/0.25 NA and 10x/0.45 NA objectives were compared for surveying an inked tissue specimen containing both normal tissue and invasive ductal carcinoma. Orange, yellow and green ink are grossly visible in the widefield image (bottom left), while each color shows up as fluorescence in one or both spectral channels in the NLM images. Both 10x and 5x objectives enable surveying the specimen in less than 1 minute, however the 5x is 2x faster and can assess tissue further from the inked margins. Scale bars: 2 mm (top, left) and 400 μ m (bottom right).

Development of Ultra-Compact Fiber Laser Nonlinear Microscopy For Low Cost and Portable Diagnostics

Initial surgical NLM system uses a tunable Titanium:Sapphire (Ti:S) laser system that weighs several hundred kilograms, is extremely costly, and requires regular maintenance, limiting its deployment to large facilities while restricting its portability. Ti:S are widely used for nonlinear imaging because of their broad tuning and ability to excite dyes fluorescing in the UV and blue region. Ytterbium fiber lasers are an alternative to standard Ti:S lasers that are widely used for industrial applications because of their low cost, extremely compact size, and excellent reliability. Unamplified, air cooled ytterbium fiber lasers, with center wavelengths of \sim 1050nm, are readily available with peak powers that enable high-speed NLM imaging as well as deeper imaging into tissue than is possible with shorter wavelength lasers.

Unfortunately, direct translation of existing histology imaging protocols to longer wavelengths is complex because of the inability to use many common dyes that are not excitable at longer wavelengths. To address this we have conducted a study of fluorine family dyes (which includes eosin) to identify eosin analogs that can be efficiently excited by ytterbium fiber lasers while emitting fluorescent light in the red part of the spectrum. We have identified several possible dyes, including sulfarhodamine, which is structurally related to the eosin and so has very similar affinity. Combined with acridine orange for nuclear contrast, sulfarhodamine labels tissue analogously to eosin while rapidly (seconds) penetrating hundreds of microns into live tissue. A further advantage of sulfarhodamine is its very low cost, with an entire surgical specimen requiring less than 5 cents of reagent while requiring substantially less labor than conventional paraffin embedded histopathology. Combined with low cost ytterbium fiber lasers, this protocol may enable histopathology to be performed for a fraction of the cost of conventional histology, and in scenarios where a complete histopathology lab is not available.

We validated the ytterbium fiber laser NLM technology by demonstrating that fresh human breast tissue could be labeled in seconds and then imaged using a low power, unamplified fiber laser. Figure 7 shows a comparison of (a) a cross-sectional NLM image and (b) a conventional paraffin-embedded H&E slide of normal breast tissue. Characteristic features of normal breast tissue can be seen on both the NLM and H&E images. Within the tissue, terminal duct lobular units (TDLUs) in the NLM images (Figure 7, green

and brown) and the H&E images (Figure 7, blue and orange) show clear correspondence. Individual acini (NLM: Figure 7, yellow; H&E: pink) and larger nonterminal ducts (NLM: Figure 7, purple; H&E: gray) are identifiable on NLM and match the H&E image. Areas of normal adipocytes and collagen are both clearly evident in NLM and H&E (inset in green and blue and in (a) and (b), respectively).

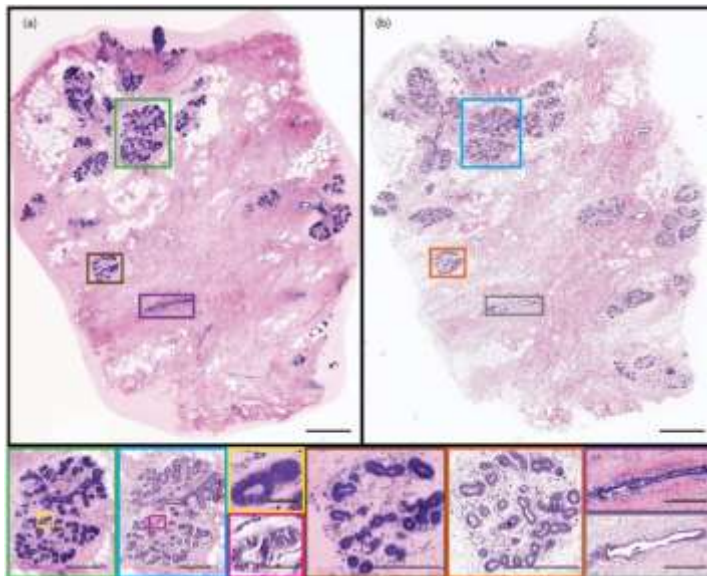


Figure 7. Normal human breast tissue (a) imaged fresh with fiber laser NLM and (b) processed using conventional H&E (500 μ m scale bar). Normal TDLUs are shown inset from the NLM (green and brown box) and in H&E (blue and orange box) (250 μ m scale bar). Individual acini (NLM: yellow box; H&E: pink box) (50 μ m scale bar) and larger ducts (NLM: brown box; H&E: gray box) (250 μ m scale bar) can also be seen.

Development of nonlinear microscopy technology for rapid assessment of prostate cancer

Prostate cancer is the second most common malignancy in American men. Positive surgical margins after radical prostatectomy to treat prostate cancer occur in an about 15% (6.5-32%)(9) of patients, and increase the risk of recurrence, local recurrence and the need for salvage treatment.(10) Frozen section analysis (FSA) during a radical prostatectomy can be unreliable at predicting histologically positive surgical margins due to incomplete sampling.(11) FSA protocols with more thorough sampling reduce the rate of positive surgical margins and increase the number of nerve-sparing surgeries which improve patient quality of life; (12) however, these sampling techniques are time intensive and require a highly optimized workflow, including multiple cryostats, technologists, and pathologists per patient, to perform. (13) Consequently improved therapy based on these protocols is too expensive for the vast majority of patients, which instead receive therapy without image guidance. The development of rapid staining and imaging protocols based around 1050nm Ytterbium fiber laser technology offer an alternative to FSA that can be performed more rapidly and at greatly lower cost, potentially enabling image guidance to be incorporated into the majority of prostatectomies. We have optimized an NLM system and imaging protocols for prostate surgery applications. Figure 8 shows NLM imaging of a radical prostatectomy specimen in which the prostate tumor has begun to invade the surrounding nerve tissue outside of the prostate. Under NLM imaging, the invasion is easily visualized even in fresh tissue, potentially enabling intraoperative assessment of prostate cancer invasion.

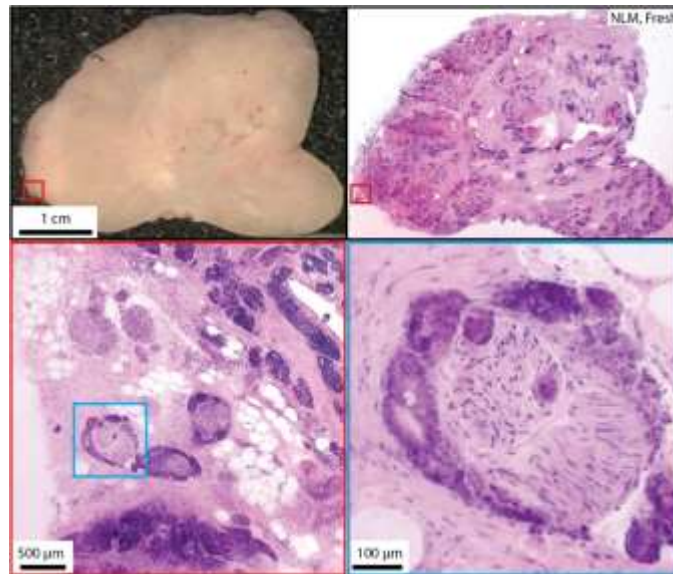


Figure 8. A white-light photograph and NLM image of a multi-centimeter, freshly excised, unfixed prostate tissue section. Extra-prostatic extension and perineural invasion is among the periprostatic fat (red and blue). (10x objective, 1 μ m pixel).

Development of nonlinear microscopy technology for rapid assessment of skin cancer

Nonmelanoma skin cancer (NMSC) is the most common form of cancer in the US, with estimates as high as 5.4 million cases in 2012 (14), more than all other forms of cancer combined (15). Furthermore, the incidence of NMSC has increased 350% over the last 2 decades (14). As a result of rapidly increasing incidence, the cost of treating NMSC now totals \$4.75 billion per year, a sum that has been increasing 15% annually (16). However, tools for rapidly performing surgical pathology in the operating room remain time-consuming and inefficient.

We are developing NLM technology for dermatopathology applications that may enable more cost-effective surgical management of skin cancer. Using frozen surgical specimens collected from patients undergoing surgery for basal cell carcinoma (BCC) at a Boston-area hospital, we rapidly imaged specimens and compared to conventional histopathology generated during each patient's surgery (Figure 9). The imaging results show that the fluorescent labeling protocol combined with VHE rendering can reproduce many of the diagnostic features of paraffin embedded histology in a clinical setting in a fraction of the normal processing time.

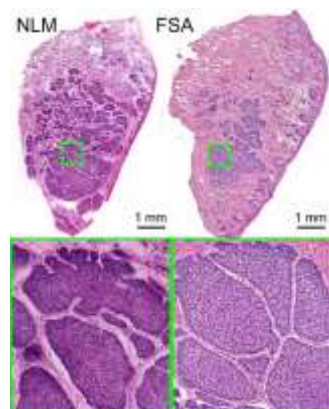


Figure 9. NLM (left) and conventional frozen section (right) of a Mohs surgical margin taken from the nose of 54 year old patient with a large skin tumor. Inset regions show large nodular BCC, which is similarly visualized in both NLM and conventional histology.

Development of extreme field size NLM imaging technology

NLM imaging requires high numerical aperture focusing for nonlinear excitation of fluorophores and rapid scanning. These requirements often necessitate the use of commercial microscope objectives that prioritize high spatial resolution at the expense of field of view, thus limiting the space-bandwidth product and throughput of conventional 2P systems. However, high throughput 2P imaging is important in a multitude of applications, including observation of functional brain activity within a hemisphere and across hemispheres of the mouse brain(17), imaging of human tissue samples for pathology assessment(18), as well as high throughput imaging and screening. Towards this goal, our group collaborated with Thorlabs to develop a custom wide field of view 2P microscope. The microscope uses customized optics to achieve a record $4\text{ mm} \times 4\text{ mm}$ square field of view at 0.5 NA for two-photon excitation. The theoretical FWHM lateral resolution of the wide-field 2P system is $0.75\ \mu\text{m}$, which can generate a 11,000 pixel x 11,000 pixel (121 MPixel) critically sampled image across the entire field. The system uses a 4 kHz resonant scanner for bidirectional fast-axis scanning (8 kHz effective line rate), and a full resolution and critically sampled frame will be able to be acquired in 1.375 seconds. Figure 10 shows the optical schematic and the setup at MIT for nonlinear microscopy studies.

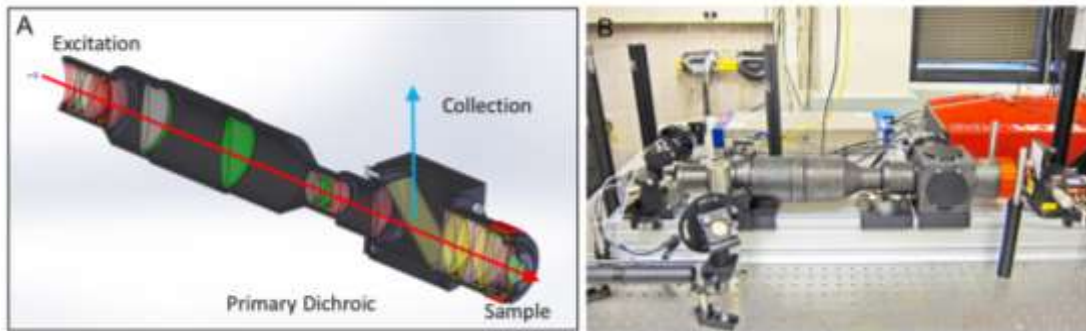


Figure 10. (A) Rendering of the custom objective for wide field 2P imaging. The objective achieves a record $4\text{mm} \times 4\text{mm}$ square field of view at 0.5 NA for two-photon excitation. (B) Wide field of view microscope being tested for optical performance at MIT.

The performance of the wide field 2P microscope was characterized using a single mode fiber at 853 nm for illumination. The excitation light was projected through the scanning mechanism and objective to generate a focused spot at the nominal location of the sample, and a secondary microscope with a higher numerical aperture was used to image the focused spot. The experimental PSF measurements were compared to the expected optical performance of the microscope simulated in ZEMAX (Figure 11). Representative experimental measurements at a field position of $x = 1\text{ mm}$, $y = 2\text{ mm}$ are in close agreement with the simulated performance. Similar agreement was found across other field positions indicating that the custom lens fabrication and optical assembly achieves the expected design performance. Additionally, a slant edge experiment was performed to assess the system modulation transfer function (MTF). A USAF 1951 was projected through the wide field 2P microscope and into the sample plane, and the image was projected to the detector of a secondary microscope with magnification and higher resolution. An ISO 12233 slant edge MTF test demonstrated close agreement between the experimental slant edge results and the predicted simulated results.

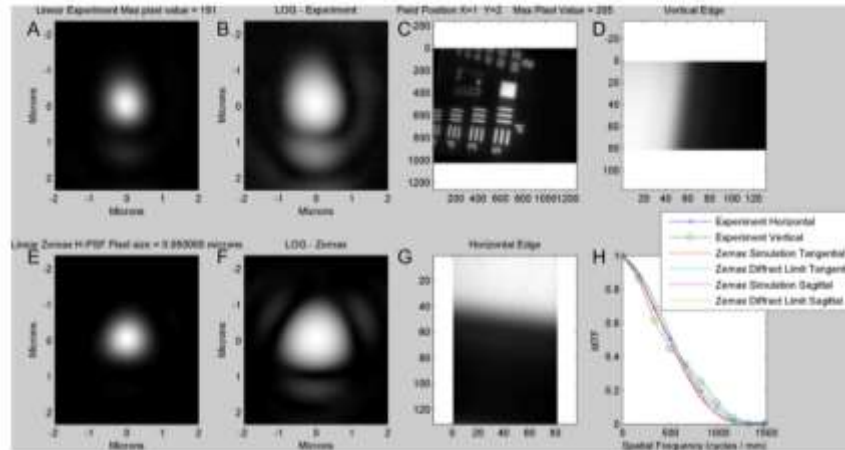


Figure 11. Simulated and experimental optical performance of the wide field 2P microscope. (A-B) Point spread function (PSF) experimental measurements at one field position demonstrate close agreement with simulated PSFs generated in ZEMAX (E-F). (C-D) and (G-H) Slanted edge test to assess the modulation transfer function (MTF) of the system. (H) Shows the experimentally measured MTF and simulated MTF. The close agreement indicates that the optical elements and assembly achieve the design performance in spite of the high complexity of this system.

We have also performed a preliminary demonstration of 2P wide-field imaging using a fixed human breast tissue with a 800 nm Ti:Sapphire femtosecond laser for excitation. Figure 12 shows a 5000 pixel \times 5000 pixel image of the tissue stained with DAPI and eosin for nuclear and stromal contrast, respectively. The system detection currently supports only one fluorescence channel, so two fluorescence images were acquired sequentially to generate the dual color 2P image shown in Figure 12A. Fluorescence filters with passbands corresponding to the DAPI and eosin emission spectra were used to isolate the fluorescence signal from each fluorophore. The fluorescence intensity image was then remapped to a color space resembling conventional H&E histology using a physically realistic light attenuation model termed virtual trans-illumination microscopy(8). The remapped full 2P image and digitally zoomed view of regions of interest are shown in Figure 12 (B-D). This wide field imaging system will be enabling for imaging studies of challenging spatial-temporal biological events and high throughput imaging of brain, small animal and human tissue samples. The next steps of the program are to develop software and multichannel detection and then to apply the microscope for tissue and in vivo neuroscience investigations. This project represents a several hundred thousand dollar investment from industry and the commercialization of wide field 2P microscopy technology promises to accelerate progress in neurosciences as well as multiple other fields which use nonlinear microscopy.

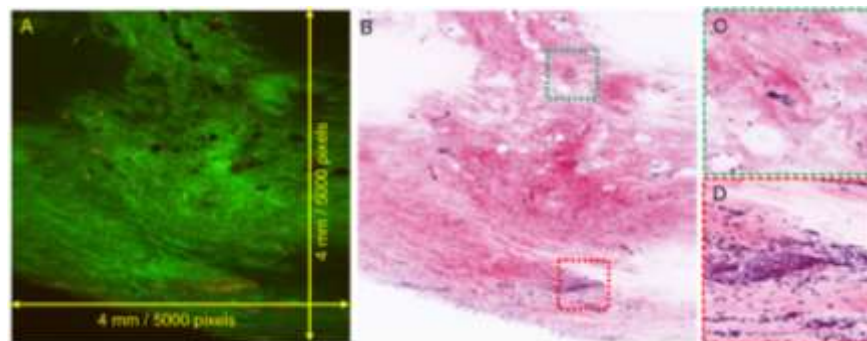


Figure 12. Wide field of view 2P images taken of human breast tissue with the prototype microscopy instrument. (A) Tissue labeled with DAPI (red) and eosin (green) showing a 4 mm by 4 mm field imaged at 25 MP resolution. (B) Same image rendered as a virtual H&E histology slide. (C) Region of normal stroma. (D) Transected view of a breast duct. This example demonstrates a record field of view within a single image. This technology promises to have multiple applications in neurosciences, tissue imaging and high throughput screening.

Development of ultra-low cost histology technology using immersion microscopy with ultraviolet surface excitation (MUSE)

NLM can image intact tissues without complex preparation, which is ideal for rapid evaluation of surgical or biopsy specimens, but requires costly femtosecond lasers and scanning optics, limiting its use in low resource or field deployable equipment. An alternative approach, called microscopy with ultraviolet surface excitation (MUSE), was recently proposed by Levenson and Demos(19). In this approach, optical sectioning is achieved by the strong absorption of deep ultraviolet (DUV) illumination light, which limits fluorescent excitation primarily to the tissue surface. MUSE enables simple, compact and extremely robust imaging schemes such as LED illuminators and conventional optical microscopes without requiring large and complex femtosecond lasers or beam scanning. Because of the extremely simple optical design, the construction of low cost, light weight and handle held MUSE technology is dramatically more simple than alternative technologies such as NLM or OCT. Consequently, MUSE may be a valuable imaging technology for field or point of care diagnostics where access to large histology facilities is limited.

Water immersion MUSE and co-registered MUSE/NLM imaging system

MUSE uses DUV (around 280 nm wavelength) excitation which is strongly absorbed by proteins in human tissue. The depth of fluorescence excitation is determined in part by the tangential component of the illumination, which can be decreased by illuminating at a high angle. However, the improvement in optical sectioning thickness from high angle illumination is limited by refraction at the tissue interface (Figure 13a). Human tissue has a refractive index (n) similar to or greater than water (tissue: typical $n=1.4$, water: $n=1.353$ at 280 nm)(20), therefore, using water immersion will enable a steeper illumination angle relative to the surface normal (Figure 13a). Table 1 summarizes the angle of refraction and relative axial penetration depth of DUV light for a 70-degree illumination angle. At this angle, water immersion MUSE should achieve a ~50% reduction in optical sectioning thickness for typical human tissue compared with air immersion MUSE.

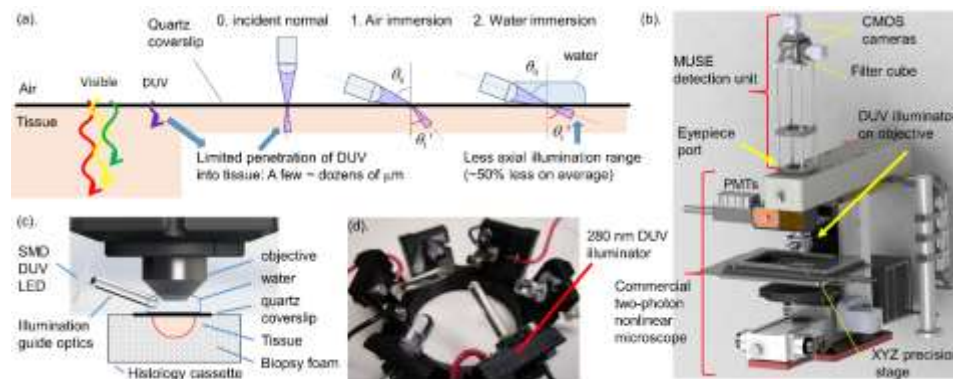


Figure 13. Principle of MUSE optical sectioning and MUSE imaging system. (a) The depth of illumination penetration into tissue decreases with wavelength and with increasing illumination angle. Higher index immersion media enables high incident angle illumination, reducing the optical sectioning thickness. (b) Drawing of the co-registered MUSE/NLM imaging system. The MUSE imaging unit was connected to the eyepiece port of a commercial NLM system to compare MUSE images with corresponding high resolution NLM. Dual channel imaging using fluorescence filters is used for both MUSE and NLM, while a precision linear motor translation stage enables mosaic imaging. Spectrally separated fluorescence is detected by CMOS cameras (MUSE) or PMTs (NLM). The DUV illuminator is mounted on the microscope objective. (c) Schematic of DUV illuminator with tissue specimen immobilized in a histology cassette with a quartz coverslip window and saline-soaked biopsy foam. (d) Photo of the illuminator with three DUV sapphire lightguides for MUSE and three visible LEDs for alignment.

We designed a water immersion DUV illuminator using surface mount LEDs and DUV illumination guiding optics for high incident angle illumination. We built a dual camera fluorescence imaging module

which attached to the microscope eyepiece port of a commercial NLM system (Figure 13b) and mounted 3D printed DUV illuminators on the objective (Figure 13c,d), enabling MUSE imaging co-registered to NLM(21).

Table 1. Relation of illumination angle and penetration depth of DUV light into human tissue (Tissue $n=1.4$). The range of geometrically possible illumination angles (viewing angle to the edge of illuminator) for the system used in this paper is shown along with the central angle.

	0. normal	1. Air immersion	2. Water immersion
Angle of incidence: θ_0 (degree)	0	70 ($58 < \theta_0 < 83$)	70 ($58 < \theta_0 < 83$)
Angle of refraction: θ_1' (degree)	0	42 ($37 < \theta_1' < 45$)	63 ($55 < \theta_1' < 74$)
Normalized axial penetration depth: $z = \cos \theta_1'$	1	0.74 ($0.71 < z < 0.80$)	0.45 ($0.28 < z < 0.57$)

Quantitative assessment of optical sectioning thickness in MUSE

Measuring the effective optical sectioning thickness in MUSE is challenging because the layer of tissue imaged is on the outmost surface, and the optical section thickness depends on the tissue properties which can vary locally. To determine the optical sectioning thickness of MUSE in human tissue, we developed a measurement technique that images individual cell nuclei sparsely located at different depths. In this technique, the depths of nuclei are measured precisely using volumetric high resolution femtosecond NLM images, and then the same tissue specimens are imaged using MUSE. By correlating the signal intensity measured with MUSE with the depth information obtained from volumetric NLM, the reduction in MUSE signal as a function of depth below the tissue surface can be computed. Furthermore, by measuring an ensemble of nuclei, random variations in local tissue absorption or nuclei brightness can be averaged to determine an effective overall measure of MUSE optical sectioning.

This method was applied to fresh, unfixed benign human breast tissue (Figure 14a). Figure 14c shows a bar plot of the median and range (25-75 percentile) of signal intensities from nuclei for air and water immersion MUSE as a function of depth. The solid line fits were calculated by modeling the nuclei fluorescence as a combination of a DUV excitation term following Beer's law and a constant background fluorescence term; (I_0 : constant background fluorescence, z : depth of nuclei, e^{-1} depth). The average calculated e^{-1} depths were 10 μm for water immersion and 20 μm for air immersion MUSE, consistent with a 50% improvement in optical sectioning expected from water immersion illumination.

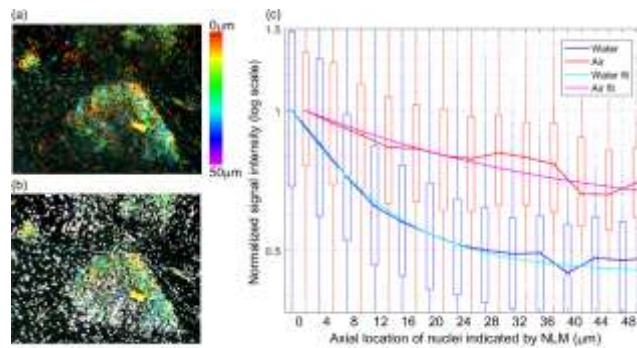


Figure 14. Quantitative assessment of optical sectioning thickness in MUSE. (a) Volumetric NLM images of fresh, unfixed benign breast tissue ($\sim 1 \text{ mm}^2$) were used to measure the depth of nuclei observed in MUSE. Tissue was stained with PI/EY in water; but only the PI channel signal was used for this analysis. Isolated nuclei were segmented ((b), white areas. Total 0.3 mm^2) and the signal intensity of nuclei in co-registered water immersion and air immersion MUSE images were calculated as a function of depth measured by NLM. (c) Box plot of the signal intensities for each depth shows that water immersion MUSE suppresses signal from nuclei deep inside tissue substantially more than air immersion MUSE. Boxes shows 25-75% range, solid lines show median, and small dots show outliers. Fitting curves indicate that the e^{-1} depths are 10 μm (water immersion MUSE) and 20 μm (air immersion MUSE).

Example MUSE images of freshly excised, unfixed specimens

Figure 15 shows a comparison of air and water immersion MUSE, NLM and conventional formalin fixed paraffin embedded H&E histology of freshly excised normal skin and normal breast tissue. PI/EY in 70% ethanol was used for MUSE and NLM fluorescent staining. The skin images (Figure 15a-d) show that MUSE reproduces the appearance of the normal epidermis layer in H&E and is consistent with NLM images. This is an important finding because it suggests that MUSE may be useful in dermatology imaging for example, in surgery for Basal cell carcinoma.

Conversely, the breast images (Figure 15e-h) show that MUSE poorly resolves the structure of normal terminal ductal lobular units, compared with standard H&E histology (Figure 15e,h) or NLM images. This loss of image quality occurs because MUSE has a thick optical sectioning and high background signal compared with NLM. Water immersion MUSE (Figure 15b,f) shows improved image quality with less background signal and higher contrast than air immersion MUSE (Figure 15a,e) due to its thinner optical section.

These results indicate that water immersion illumination improves MUSE performance and that MUSE is a promising low-cost imaging modality for rapid histological evaluation of freshly excised tissue specimens. Imaging tissue pathology without the need to physically section (microtome) specimens is a powerful advantage for imaging surgical specimens to assess margin status. MUSE applications may be limited to specific types of pathologies where thicker optical sectioning does not appreciably degrade image quality, however the low cost and simplicity of the imaging system promise to be a powerful advantage for many biological and clinical applications.

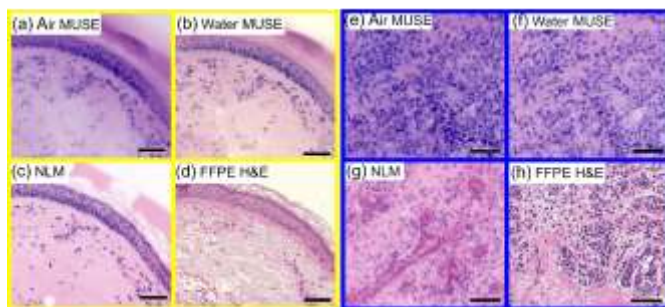


Figure 15. Imaging of fresh excised, normal human skin specimen with (a) air immersion MUSE, (b) water immersion MUSE, (c) NLM and (d) formalin fixed paraffin embedded H&E. The appearance of the normal epidermis layer can be seen using each modality, while the thinner optical sectioning of water immersion MUSE enables visualization of finer details than air immersion. Imaging of normal breast specimen with (e) air immersion MUSE, (f) water immersion MUSE, (g) NLM and (h) formalin fixed paraffin embedded H&E. The normal terminal ductal lobular unit structures such as connecting ducts can be seen. The thicker optical sectioning in MUSE limits accurate visualization of lobular structures which would be important for assessing surgical cancer specimens. Scale bar 100 μm (a-d), 50 μm (e-h).

References

1. Helmchen F, Denk W. Deep tissue two-photon microscopy. *Nat Methods*. 2005;2(12):932-40. doi: Doi 10.1038/Nmeth818. PubMed PMID: ISI:000233767700015.
2. Zipfel WR, Williams RM, Christie R, Nikitin AY, Hyman BT, Webb WW. Live tissue intrinsic emission microscopy using multiphoton-excited native fluorescence and second harmonic generation. *Proceedings of the National Academy of Sciences of the United States of America*. 2003;100(12):7075-80. Epub 2003/05/21. doi: 10.1073/pnas.0832308100. PubMed PMID: 12756303; PMCID: 165832.
3. Provenzano PP, Inman DR, Eliceiri KW, Knittel JG, Yan L, Rueden CT, White JG, Keely PJ. Collagen density promotes mammary tumor initiation and progression. *BMC Med*. 2008;6:11. Epub 2008/04/30. doi: 1741-7015-6-11 [pii] 10.1186/1741-7015-6-11. PubMed PMID: 18442412; PMCID: 2386807.

4. Provenzano PP, Eliceiri KW, Campbell JM, Inman DR, White JG, Keely PJ. Collagen reorganization at the tumor-stromal interface facilitates local invasion. *BMC Med.* 2006;4(1):38. Epub 2006/12/28. doi: 1741-7015-4-38 [pii] 10.1186/1741-7015-4-38. PubMed PMID: 17190588; PMCID: 1781458.
5. Schnitt SJ. The diagnosis and management of pre-invasive breast disease: flat epithelial atypia--classification, pathologic features and clinical significance. *Breast Cancer Res.* 2003;5(5):263-8. Epub 2003/08/21. doi: 10.1186/bcr625. PubMed PMID: 12927037; PMCID: 314429.
6. Meng S, Tripathy D, Frenkel EP, Shete S, Naftalis EZ, Huth JF, Beitsch PD, Leitch M, Hoover S, Euhus D, Haley B, Morrison L, Fleming TP, Herlyn D, Terstappen LW, Fehm T, Tucker TF, Lane N, Wang J, Uhr JW. Circulating tumor cells in patients with breast cancer dormancy. *Clin Cancer Res.* 2004;10(24):8152-62. Epub 2004/12/30. doi: 10/24/8152 [pii] 10.1158/1078-0432.CCR-04-1110. PubMed PMID: 15623589.
7. Giacomelli MG, Yoshitake T, Cahill LC, Vardeh H, Quintana LM, Faulkner-Jones BE, Brooker J, Connolly JL, Fujimoto JG. Multiscale Nonlinear Microscopy and Widefield White Light Imaging Enables Rapid Histological Imaging of Surgical Specimen Margins. *Biomedical Optics Express.* 2018; In press.:1209-15.
8. Giacomelli MG, Husvogt L, Vardeh H, Faulkner-Jones BE, Hornegger J, Connolly JL, Fujimoto JG. Virtual Hematoxylin and Eosin Transillumination Microscopy Using Epi-Fluorescence Imaging. *Plos One.* 2016;11:e0159337. doi: 10.1371/journal.pone.0159337.
9. Yossepowitch O, Briganti A, Eastham JA, Epstein J, Graefen M, Montironi R, Touijer K. Positive surgical margins after radical prostatectomy: A systematic review and contemporary update. *European Urology.* 2014;65:303-13. doi: 10.1016/j.eururo.2013.07.039. PubMed PMID: 23932439.
10. Boorjian SA, Karnes RJ, Crispen PL, Carlson RE, Rangel LJ, Bergstralh EJ, Blute ML. The Impact of Positive Surgical Margins on Mortality Following Radical Prostatectomy During the Prostate Specific Antigen Era. *The Journal of Urology.* 2010;183:1003-9. doi: 10.1016/j.juro.2009.11.039. PubMed PMID: 20092854.
11. Gillitzer R, Thuroff C, Fandel T, Thomas C, Thuroff JW, Brenner W, Wiesner C, Jones J, Hansen T, Hampel C. Intraoperative peripheral frozen sections do not significantly affect prognosis after nerve-sparing radical prostatectomy for prostate cancer. *BJU International.* 2011;107:755-9. doi: 10.1111/j.1464-410X.2010.09591.x. PubMed PMID: 20880193.
12. Beyer B, Schlomm T, Tennstedt P, Boehm K, Adam M, Schiffmann J, Sauter G, Wittmer C, Steuber T, Graefen M, Huland H, Haese A. A feasible and time-efficient adaptation of NeuroSAFE for da Vinci robot-assisted radical prostatectomy. *European Urology.* 2014;66:138-44. doi: 10.1016/j.eururo.2013.12.014. PubMed PMID: 24411279.
13. Vasdev N, Agarwal S, Rai BP, Soosainathan A, Shaw G, Chang S, Prasad V, Mohan-S G, Adshead JM. Intraoperative Frozen Section of the Prostate Reduces the Risk of Positive Margin Whilst Ensuring Nerve Sparing in Patients with Intermediate and High-Risk Prostate Cancer Undergoing Robotic Radical Prostatectomy: First Reported UK Series. *Current Urology.* 2016;9:93-103. doi: 10.1159/000442860. PubMed PMID: 27390582.
14. Rogers HW, Weinstock Ma, Feldman SR, Coldiron BM. Incidence Estimate of Nonmelanoma Skin Cancer (Keratinocyte Carcinomas) in the US Population, 2012. *JAMA dermatology.* 2015;06360:1081-6. doi: 10.1001/jamadermatol.2015.1187. PubMed PMID: 25928283.
15. American Cancer Society: Cancer Facts & Figures 2012.
16. Guy GP, Machlin SR, Ekwueme DU, Yabroff KR. Prevalence and costs of skin cancer treatment in the U.S., 2002-2006 and 2007-2011. *American Journal of Preventive Medicine.* 2015;48:183-7. doi: 10.1016/j.amepre.2014.08.036. PubMed PMID: 25442229.

17. Stirman JN, Smith IT, Kudenov MW, Smith SL. Wide field-of-view, multi-region, two-photon imaging of neuronal activity in the mammalian brain. *Nature Biotechnology*. 2016;34:857-62. doi: 10.1038/nbt.3594. PubMed PMID: 27347754.
18. Tao YK, Shen D, Sheikine Y, Ahsen OO, Wang HH, Schmolze DB, Johnson NB, Brooker JS, Cable aE, Connolly JL, Fujimoto JG. Assessment of breast pathologies using nonlinear microscopy. *Proceedings of the National Academy of Sciences*. 2014;111:15304-9. doi: 10.1073/pnas.1416955111.
19. Fereidouni F, Harmany ZT, Tian M, Todd A, Kintner JA, Mcpherson JD, Borowsky AD, Bishop J, Lechpammer M, Demos SG, Levenson R. Microscopy with ultraviolet surface excitation for rapid slide-free histology. *Nature Biomedical Engineering*. 2017. doi: 10.1038/s41551-017-0165.
20. Tsenova V, Stoykova E. Refractive index measurement in human tissue samples. *Proc SPIE 5226, 12th International School on Quantum Electronics: Laser Physics and Applications*. 2003:413. doi: 10.1117/12.519584.
21. Yoshitake T, Giacomelli MG, Quintanna L, Vardeh H, Cahill L, Faulkner-Jones BE, Connolly JL, Do D, Fujimoto JG. Rapid histopathological imaging of skin and breast cancer surgical specimens using immersion microscopy with ultraviolet surface excitation. *Scientific Reports*. 2018; 8.

Publications under AFOSR Contract FA9550-12-1-0499

10/1/2012– 3/29/2018

1. A. Khilo, S. J. Spector, M. E. Grein, A. H. Nejadmalayeri, Ch. W. Holzwarth, M. Y. Sander, M. S. Dahlem, M. Y. Peng, M. W. Geis, N. A. DiLello, J. U. Yoon, A. Motamedi, J. S. Orcutt, J. P. Wang, Ch. M. Sorace-Agaskar, M.A. Popović, J. Sun, G. R. Zhou, H. Byun, J. Chen, J. L. Hoyt, H. I. Smith, R. J. Ram, M. Perrott, Th. M. Lyszczarz, E. P. Ippen, and F. X. Kärtner, “Photonic ADC: overcoming the bottleneck of electronic jitter,” *Opt. Express* 20:(4) 4454-4469 (2012).
2. W. Choi, B. Baumann, E.A. Swanson, and J.G. Fujimoto, “Extracting and compensating dispersion mismatch in ultrahigh-resolution Fourier domain OCT imaging of the retina,” *Opt. Exp.* 20, 25357-25368, 2012
3. E. Granados, L-J. Chen, C-J. Lai, K-H. Hong, F. X. Kärtner, “Wavelength scaling of optimal hollow-core fiber compressors in the single-cycle limit,” *Optics Express* 20:(8), pp.9099-9108 (2012).
4. D. Li, U. Demirbas, A. Benedick, A. Sennaroglu, J. G. Fujimoto and F. X. Kärtner, “Attosecond timing jitter pulse trains from semiconductor saturable absorber mode-locked Cr:LiSAF lasers,” *Opt. Express* 20: (21), pp. 23422-23435 (2012).
5. W. P. Putnam, D. N. Schimpf, G. Abram, F. X. Kärtner, “Bessel-Gauss beam enhancement cavities for high-intensity applications”, *Opt. Express* 20, 24429 (2012).
6. D. N. Schimpf, J. Schulte, W. P. Putnam, F. X. Kärtner, “Generalizing higher-order Bessel-Gauss beams: analytical description and demonstration”, *Opt. Express* 20, 26852 (2012).
7. J. A. Cox, W. P. Putnam, A. Sell, A. Leitenstorfer, F. X. Kärtner, “Pulse synthesis in the single-cycle regime from independent mode-locked lasers using attosecond-precision feedback”, *Opt. Lett.* 37, 3579 (2012).
8. I. Grulkowski, J.J. Liu, B. Potsaid, V. Jayaraman, C.D. Liu, J. Jiang, A.E. Cable, J.S. Duker, and J.G. Fujimoto, “Retinal, anterior segment and full eye imaging using ultrahigh speed swept source OCT with vertical-cavity surface emitting laser,” *Biomed. Opt. Exp.* 3, 2733-2751, 2012
9. D. Keathley, A. Sell, W.P. Putnam, S. Guerrero, L. Velásquez-García, and F.X. Kärtner, "Strong-field photoemission from silicon field emitter arrays," *Ann. Phys.* 525:(1-2), 144-150 (2013).
10. J. Lim, H.-W. Chen, G. Chang, and F.X. Kärtner, "Frequency comb based on a narrowband Yb-fiber oscillator: pre-chirp management for self-referenced fCEO stabilization," *Opt Express.* 21:(4), 4531-4538 (2013).
11. S.-H. Huang, E. Granados, W. R. Huang, K.-H. Hong, L. E. Zapata and F. X. Kärtner, “High conversion efficiency, high energy terahertz pulses by optical rectification in cryogenically cooled lithium niobate,” *Opt. Lett.* 38:(5), 796-798 (2013).

12. L. J. Wong, A. Fallahi and F. X. Kärtner, "Compact Electron Acceleration and Bunch Compression in THz Waveguides," *Opt. Express* 21, p. 9792 (2013).
13. W. Choi, B. Potsaid, V. Jayaraman, B. Baumann, I. Grulkowski, J.J. Liu, C.D. Lu, A.E. Cable, D. Huang, J.S. Duker, and J.G. Fujimoto, "Phase-sensitive swept-source optical coherence tomography imaging of the human retina with a vertical cavity surface-emitting laser light source," *Opt. Lett.* 38, 338-340, February 2013.
14. J.J. Liu, I. Grulkowski, M.F. Kraus, B. Potsaid, C.D. Lu, B. Baumann, J.S. Duker, J. Hornegger, and J.G. Fujimoto, "In vivo imaging of the rodent eye with swept source/Fourier domain OCT," *Biomed. Opt. Exp.* 4, 351-363, February 2013.
15. M. Y. Peng, P. T. Callahan, S. Valente, M. Xin, L. Grüner-Nielsen, E. Monberg, M. Yan, J. M. Fini, and F. X. Kärtner, "Sub-Femtosecond Timing Distribution via a 1.2-km Polarization-Maintaining Fiber Link: Approaching 10-21 Link Stability," *Opt. Exp.* 21:(17), 19982-19989 (2013).
16. I. Grulkowski, J.J. Liu, B. Potsaid, V. Jayaraman, J. Jiang, J.G. Fujimoto, and A.E. Cable, "High-precision, high-accuracy, ultralong-range swept-source optical coherence tomography using vertical cavity surface-emitting laser light source," *Opt. Lett.* 38, 673-675, March 2013.
17. W. R. Huang, S.W. Huang, E. Granados, R. Koustuban, K-H. Hong, L. E. Zapata, and F. X. Kärtner, "Highly efficiency THz pulse generation by optical rectification in stoichiometric and cryo-cooled congruent lithium niobate," *J. Mod. Optics* DOI:10.1080/09500340.2013.868547
18. S. Bhardwaj, S. K. Son, K.-H. Hong, C-J. Lai, F. X Kärtner, and R. Santra, "Recombination Amplitude of Noble Gases, in Length and Acceleration Form, beyond Strong Field Approximation," *Phys. Rev. A* 88, 053405 (2013).
19. X. Fu, K.-H. Hong, L.-J. Chen, and F. X. Kärtner, "Performance scaling of high-power picosecond cryogenically-cooled Yb:YAG multipass amplification," *J. Opt. Soc. Am. B* 30, 2798-2808 (2013).
20. A. Li, O.O. Ahsen, J.J. Liu, C. Du, M.L. McKee, W. Wasco, C.H. Newton-Cheh, C.J. O'Donnell, J.G. Fujimoto, C. Zhou, and R.E. Tanzi, "Silencing of the Drosophila ortholog of SOX5 in heart leads to cardiac dysfunction as detected by optical coherence tomography," *Hum. Mol. Gen.* 22, 3798-3806, (2013).
21. T-H. Tsai, B. Potsaid, Y.K. Tao, V. Jayaraman, J. Jiang, P.J.S. Heim, M.F. Kraus, C. Zhou, J. Hornegger, H. Mashimo, A.E. Cable, and J.G. Fujimoto, "Ultrahigh speed endoscopic optical coherence tomography using micromotor imaging catheter and VCSEL technology," *Biomed. Opt. Exp.* 4, 1119-1132, (2013).
22. C.-J. Lai, G. Cirmi, K.-H. Hong, J. Moses, S.W. Huang, E. Granados, P. Keathley, S. Bhardwaj, and F. X. Kärtner, "Wavelength scaling of high harmonic generation close to the multiphoton ionization regime," *Phys. Rev. Lett.* 111, 073901 (2013).

23. C. C. Evans, K. Shtyrkova, J.D.B. Bradley, O. Reshef, E. Ippen and E. Mazur, "Spectral broadening in anatase titanium dioxide waveguides at telecommunication and near-visible wavelengths," *Opt. Exp.*, 21, pp.18582-18591 (2013)
24. O.O. Ahsen, Y.K. Tao, B.M. Potsaid, Y. Sheikine, J. Jiang, I. Grulkowski, T-H. Tsai, V. Jayaraman, M.F. Kraus, J.L. Connolly, J. Hornegger, A. Cable, and J.G. Fujimoto, "Swept source optical coherence microscopy using a 1310 nm VCSEL light source," *Opt. Exp.* 21, 18021-18033, (2013).
25. H-C. Lee, J.J. Liu, Y. Sheikine, A.D. Aguirre, J.L. Connolly, and J.G. Fujimoto, "Ultrahigh speed spectral-domain optical coherence microscopy," *Biomed. Opt. Exp.* 4, 1236-1254, (2013).
26. D. N. Schimpf, W. P. Putnam, M.D.W Grogan, S. Ramachandran, and F.X. Kärtner, "Radially polarized Bessel-Gauss beams: decentered Gaussian beam analysis and experimental verification," *Optics Express*, Vol. 21 Issue 15, pp.18469-18483 (2013)
27. D. Keathley, A. Sell, W.P. Putnam, S. Guerrero, L. Velásquez-García, and F.X. Kärtner, "Strong-field photoemission from silicon field emitter arrays," *Ann. Phys.* 525:(1-2), 144-150 (2013).
28. S. P. Nabanja, L. A. Kolodziejcki, G. S. Petrich, M. Y. Sander, J. L. Morse, K. Shtyrkova, E. P. Ippen and F. X. Kärtner, "Large-area broadband saturable Bragg reflectors using oxidized AlAs in the circular and inverted mesa geometries," *J. Appl. Phys.* 113, 163102 (2013)
29. H. Suchowski, P. R. Krogen, S.-W. Huang, F. X. Kärtner, and J. Moses, "Octave-spanning Coherent Mid-IR Generation via Adiabatic Difference Frequency Conversion," *Opt. Express* 21, 28892 (2013).
30. S. Carbajo, E. Granados, D. Schimpf, A. Sell, K.-H. Hong, J. Moses, and F. X. Kärtner, "Efficient generation of ultra-intense few-cycle radially polarized laser pulses." *Opt. Lett.* 39:(8), pp. 2487-2490 (2014).
31. A. Sell, and F. X. Kärtner, "Attosecond electron bunches accelerated and compressed by radially polarized laser pulses and soft-X-ray pulses from optical undulators," *J. Phys. B* 47, p. 015601 (2014), doi:10.1088/0953-4075/47/1/015601.
32. M. Adhi, J.J. Liu, A.H. Qavi, I. Grulkowski, J.G. Fujimoto, and J.S. Duker, "Enhanced visualization of choroido-scleral interface using swept-source OCT," *Ophthalmic Surg. Lasers Imaging Retina*, 44, S40-S42, November/December 2013.
33. I. Grulkowski, J.J. Liu, J.Y. Zhang, B. Potsaid, V. Jayaraman, A.E. Cable, J.S. Duker, and J.G. Fujimoto, "Reproducibility of a long-range swept-source optical coherence tomography ocular biometry system and comparison with clinical biometers," *Ophthalmology* 120, 2184-2190, November 2013
34. W. Choi, K.J. Mohler, B. Potsaid, C.D. Lu, J.J. Liu, V. Jayaraman, A.E. Cable, J.S. Duker, R. Huber, and J.G. Fujimoto, "Choriocapillaris and choroidal microvasculature imaging with ultrahigh speed OCT angiography," *PLOS One* 8, e81499, December 2013.

35. C.D. Lu, M.F. Kraus, B. Potsaid, J.J. Liu, W. Choi, V. Jayaraman, A.E. Cable, J. Hornegger, J.S. Duker, and J.G. Fujimoto, "Handheld ultrahigh speed swept source optical coherence tomography instrument using a MEMS scanning mirror," *Biomed. Opt. Exp.* 5, 293-311, January 2014.
36. M. Xin, K. Safak, M. Y. Peng, P. T. Callahan and F. X. Kärtner, "One-femtosecond, long-term stable remote laser synchronization over a 3.5-km fiber link," *Opt. Exp.* 22:(12) 14904 (2014). | DOI:10.1364/OE.22.014904.
37. M. E. Swanwick, P. D. Keathley, A. Fallahi, P. R. Krogen, G. Laurent, J. Moses, F. X. Kärtner, and L. F. Velásquez-García, "Nanostructured Ultrafast Silicon-Tip Optical Field-Emitter Arrays," *Nano Lett.*, 14:(9), pp 5035–5043 (2014).
38. R. Koustuban, W. R. Huang, S. Carbajo, X. Wu and F. X. Kärtner, "Limitations to THz generation by optical rectification using tilted pulse fronts," *Opt. Express* 22, 20239 (2014).
39. X. Wu, S. Carbajo, R. Koustuban, F. Ahr, G. Cirimi, Y. Zhou, O. D. Mücke and F. X. Kärtner, "Terahertz Generation in Lithium Niobate Driven by Ti:Sapphire Laser Pulses and its Limitations," *Opt. Lett.* 39:(18), pp. 5403-5406 (2014).
40. K. H. Hong, C. J. Lai, J. P. Siqueira, P. Krogen, J. Moses, C.-L. Chang, G. J. Stein, L. E. Zapata and F. X. Kärtner, "Multi-mJ, kHz, 2.1- μ m optical parametric chirped-pulse amplifier and high-flux soft X-ray high-harmonic generation," *Opt. Lett.* 39:(11), pp. 3145-3148 (2014).
41. M. Y. Peng, A. Kalaydzhyan, F. X. Kärtner, "Balanced optical-microwave phase detector for sub-femtosecond optical-RF synchronization," *Optics Express*, 22:(22) pp.27102-27111 (2014).
42. P. T. Callahan, K. Safak, P. Battle, T. D. Roberts, F. X. Kärtner, "Fiber-coupled balanced optical cross-correlator using PPKTP waveguides," *Optics Express* 22:(8), pp.9749-9758 (2014).
43. N. Zhang, T-H. Tsai, O.O. Ahsen, K. Liang, H.-C. Lee, P. Xue, X. Li, and J.G. Fujimoto, "Compact piezoelectric transducer fiber scanning probe for optical coherence tomography," *Opt. Lett.* 39, 186-188, January 2014.
44. J.G. Fein, L.A. Branchini, V. Manjunath, C.V. Regatieri, J.G. Fujimoto, and J.S. Duker, "Analysis of short-term change in subfoveal choroidal thickness in age-related macular degeneration using optical coherence tomography," *Ophthalmic Surg. Lasers Imaging Retina* 45, 32-37, January/February 2014.
45. A-L. Calendron, H. Çankaya, F. X. Kärtner, "High-energy kHz Yb:KYW dual-crystal regenerative amplifier," *Optics Express*, Vol. 22 Issue 20, pp.24752-24762 (2014).
46. D. Ferrara, K.J Mohler, N. Waheed, M. Adhi, J.J Liu, I. Grulkowski, M.F Kraus, C. Baumal, J. Hornegger, J.G Fujimoto, and J.S. Duker, "En face enhanced-depth swept-source optical coherence tomography features of chronic central serous chorioretinopathy," *Ophthalmology* 121, 719-726, March 2014.

47. T-H. Tsai, J.G. Fujimoto, and H. Mashimo, "Endoscopic optical coherence tomography for clinical gastroenterology," *Diagnostics* 4, 57-93, May 2014.
48. M. Adhi, J.J. Liu, A.H. Qavi, I. Grulkowski, C.D. Lu, K.J. Mohler, D. Ferrara, M.F. Kraus, C.R. Bauman, A.J. Witkin, N.K. Waheed, J. Hornegger, J.G. Fujimoto, and J.S. Duker, "Choroidal analysis in healthy eyes using swept-source optical coherence tomography compared to spectral domain optical coherence tomography," *Am. J. Ophthalmol.*, 157, 1272-1281, June 2014.
49. M.F. Kraus, J.J. Liu, J. Schottenham, C-L. Chen, A. Budai, L. Branchini, T. Ko, H. Ishikawa, G. Wollstein, J. Schuman, J.S. Duker, J.G. Fujimoto, and J. Hornegger, "Quantitative 3D-OCT motion correction with tilt & illumination correction, robust similarity measure and regulation," *Biomed. Opt. Exp.* 5, 2591-2613, July 2014.
50. J.J. Liu, A.J. Witkin, M. Adhi, I. Grulkowski, M.F. Kraus, A-H. Dhalla, C.D. Lu, J. Hornegger, J.S. Duker, and J.G. Fujimoto, "Enhanced vitreous imaging in healthy eyes using swept source optical coherence tomography," *PLoS One* 9(7), e102950-1—10, July 2014.
51. Z. Wang, H-C. Lee, O.O. Ahsen, B. Lee, W. Choi, B. Potsaid, J. Liu, V. Jayaraman, A. Cable, M.F. Kraus, K. Liang, J. Hornegger, and J.G. Fujimoto, "Depth-encoded all-fiber swept source polarization sensitive OCT" *Biomed. Opt. Exp.* 5, 2931-2949, August 2014
52. T. Alasil, M. Adhi, J.J. Liu, J.G. Fujimoto, J.S. Duker, and C.R. Bauman, "Spectral-domain and swept-source OCT imaging of asteroid hyalosis: A case report," *Ophthalmic Surg. Lasers Imaging Retina* 45, 459-461, September/October 2014.
53. O.O. Ahsen, H-C. Lee, M.G. Giacomelli, Z. Wang, K. Liang, T-H. Tsai, B. Potsaid, H. Mashimo, and J.G. Fujimoto, "Correction of rotational distortion for catheter-based en face OCT and OCT angiography," *Opt. Lett.* 39, 5973-5976, October 2014.
54. Y.K. Tao, D. Shen, Y. Sheikine, O.O. Ahsen, H.H. Wang, D.B. Schmolze, N.B. Johnson, J.S. Brooker, A.E. Cable, J.L. Connolly, and J.G. Fujimoto, "Assessment of breast cancer pathologies using nonlinear microscopy," *Proc. Natl. Acad. Sci U.S.A.* 111, 15304-15309, October 2014.
55. M. Adhi, S.P. Read, J.J. Liu, J.G. Fujimoto and J.S. Duker, "High-speed ultrahigh-resolution OCT of Bruch's membrane in membranoproliferative glomerulonephritis type 2," *Ophthalmic Surg. Lasers Imaging Retina* 45, 614-617, November/December 2014.
56. E. Moulton, W. Choi, N.K. Waheed, M. Adhi, B. Lee, C.D. Lu, V. Jayaraman, B. Potsaid, P.J. Rosenfeld, J.S. Duker, and J.G. Fujimoto, "Ultrahigh-Speed Swept-Source OCT Angiography in Exudative AMD," *Ophthalmic Surg. Lasers Imaging Retina* 45, 496-505, November/December 2014.
57. T-H. Tsai, H-C. Lee, O.O. Ahsen, K. Liang, M.G. Giacomelli, B.M. Potsaid, Y.K. Tao, V. Jayaraman, M. Figueiredo, Q. Huang, A.E. Cable, J.G. Fujimoto, and H. Mashimo, "Ultrahigh speed endoscopic optical coherence tomography for gastroenterology," *Biomed. Opt. Exp.*, 5, 4387-4404, November 2014.

58. T-H. Tsai, O.O. Ahsen, H-C. Lee, K. Liang, M. Figueiredo, Y.K. Tao, M.G. Giacomelli, B.M. Potsaid, V. Jayaraman, Q. Huang, A.E. Cable, J.G. Fujimoto, and H. Mashimo, "Endoscopic optical coherence angiography enables 3-dimensional visualization of subsurface microvasculature," *Gastroenterology* 4, 1219-1221, December 2014.
59. W. R. Huang, E. A. Nanni, A. Fallahi, P. D. Keathley, K. Ravi, K.H. Hong and Franz X. Kärtner, "An electron gun powered by single-cycle terahertz pulses, arXiv preprint arXiv:1409.8668 (2014)
60. R. Hobbs, Y. Yang, P. D. Keathley, M. E. Swanwick, L. F. Velasquez-Garcia, F. X. Kärtner, W. S. Graves, and K. K. Berggren, "High-density Au Nanorod Optical Field Emitter Arrays," *Nanotechnology*, 25, pp. 465304 – 465401 (2014).
61. K. Ravi, W. R. Huang, S. Carbajo, E. A. Nanni, D. N. Schimpf, E. P. Ippen and F. X. Kärtner, "Theory of terahertz generation by optical rectification using tilted-pulse-fronts," *Optics Express*, 23(4), 5253-5276 (2015)
62. K. Ravi, W. R. Huang, S. Carbajo, X. Wu and F. X. Kärtner, "Limitations to THz generation by optical rectification using tilted pulse fronts", *Optics Express*, 22(17),20239 (2014).
63. E. A. Nanni, W. R. Huang, K. H. Hong, K. Ravi, A. Fallahi, G. Moriena ,D. R. J. Miller and F. X. Kärtner, "Terahertz-driven linear electron acceleration", *Nature Communications* 6:8486 doi: 10.1038/ncomms9486 (2015).
64. X. Wu, S. Carbajo, K. Ravi, F. Ahr, G. Cirimi, Y. Zhou, O. D. Mücke and F. X. Kärtner, "Terahertz generation in lithium niobate driven by Ti:Sapphire laser pulses and its limitations", *Optics Letters*, 39(18), 5403 (2014)
65. O. Reshef, K. Shtyrkova, M.G. Moebius, S. Griesse-Nascimento, S. Spector C. C. Evans, E. P. Ippen, E. Mazur, "Polycrystalline anatase titanium dioxide microring resonators with negative thermo-optic coefficient," *JOSA B* 32(11) 2288-2293 (2015)
66. Kyung-Han Hong, Chien-Jen Lai, Jonathas Siqueira, Peter Krogen, Jeffrey Moses, Chun-Lin Chang, Gregory J. Stein, Luis E. Zapata, and Franz X. Kärtner, "Multi-mJ, kHz, 2.1- μ m optical parametric chirped pulse amplifier and high-flux soft X-ray high-harmonic generation," *Optics Letters* 39, 3145-3148 (June, 2014).
67. Cristian Manzoni, Oliver Mücke, Giovanni Cirimi, Shaobo Fang, Jeffrey Moses, Shu-Wei Huang, Kyung-Han Hong, Giulio Cerullo, Franz X. Kärtner, "Coherent pulse synthesis: towards sub-cycle optical waveforms (invited review)," *Laser and Photonics Reviews* 9, 129-171 (March, 2015).
68. Chun-Lin Chang, Peter Krogen, Houkun Liang, Gregory J. Stein, Jeffrey Moses, Chien-Jen Lai, Jonathas P. Siqueira, Lius E. Zapata, Franz X. Kärtner, and Kyung-Han Hong*, "Multi-mJ, kHz picosecond deep ultraviolet source," *Opt. Lett.* 40, 665 (Feb, 2015).

69. Houkun Liang, Peter Krogen, Ross Grynko, Ondrej Novak, Chun-Lin Chang, Gregory J. Stein, Darshana Weerawarne, Bonggu Shim, Franz X. Kärtner, and Kyung-Han Hong, "Three-octave-spanning supercontinuum generation and sub-two-cycle self-compression of mid-infrared filaments in dielectrics," *Opt. Lett.* 40, 106 (March, 2015).
70. Chun-Lin Chang, Peter Krogen, Kyung-Han Hong, Luis E. Zapata, Jeffrey Moses, Anne-Laure Calendron, Houkun Liang, Chien-Jen Lai, Gregory J. Stein, and Franz X. Kärtner, "High-energy, kHz, picosecond hybrid Yb-doped chirped-pulse amplifier," *Opt. Express* 23, 10132 (April, 2015).
71. Kyung-Han Hong, Chun-Lin Chang, Peter Krogen, Houkun Liang, Gregory J. Stein, Jeffrey Moses, Chien-Jen Lai, and Franz X. Kärtner, "Multi-mJ, kHz picosecond deep UV source based on a frequency-quadrupled cryogenic Yb:YAG laser," *Proc. of SPIE 9513, High-Power, High-Energy, and High-Intensity Laser Technology II*, 95130U (May, 2015).
72. Chien-Jen Lai, Kyung-Han Hong, Jonathas P. Siqueira, Peter Krogen, Chun-Lin Chang, Gregory J. Stein, Houkun Liang, Phillip D. Keathley, Guillaume Laurent, Jeffrey Moses, Luis E. Zapata, and Franz X. Kärtner, "Multi-mJ mid-infrared kHz OPCPA and Yb-doped pump lasers for tabletop coherent soft X-ray generation (invited)," *Journal of Optics* 17, 094009 (Sept, 2015).
73. Z. Wang, H. C. Lee, D. Vermeulen, L. Chen, T. Nielsen, S. Y. Park, A. Ghaemi, E. Swanson, C. Doerr, and J. Fujimoto, "Silicon photonic integrated circuit swept-source optical coherence tomography receiver with dual polarization, dual balanced, in-phase and quadrature detection," *Biomedical Optics Express*, vol. 6, pp. 2562-2574, Jul 1 2015.
74. K. Liang, G. Traverso, H. C. Lee, O. O. Ahsen, Z. Wang, B. Potsaid, M. Giacomelli, V. Jayaraman, R. Barman, A. Cable, H. Mashimo, R. Langer, and J. G. Fujimoto, "Ultrahigh speed en face OCT capsule for endoscopic imaging," *Biomed Opt Express*, vol. 6, pp. 1146-63, Apr 1 2015.
75. B. Lee, W. Choi, J. Liu, C. Lu, J. S. Schuman, G. Wollstein, J. S. Duker, N. Waheed, and J. G. Fujimoto, "Cardiac-Gated En Face Doppler Measurement of Retinal Blood Flow Using Swept Source Optical Coherence Tomography at 100,000 Axial Scans per Second," *Invest Ophthalmol Vis Sci*, vol. 56, pp. 2522-30, Apr 2015.
76. D. D. John, C. B. Burgner, B. Potsaid, M. E. Robertson, B. K. Lee, W. J. Choi, A. E. Cable, J. G. Fujimoto, and V. Jayaraman, "Wideband Electrically Pumped 1050-nm MEMS-Tunable VCSEL for Ophthalmic Imaging," *Journal of Lightwave Technology*, vol. 33, pp. 3461-3468, Aug 15 2015.
77. Y. L. Jia, S. T. Bailey, T. S. Hwang, S. M. McClintic, S. S. Gao, M. E. Pennesi, C. J. Flaxel, A. K. Lauer, D. J. Wilson, J. Hornegger, J. G. Fujimoto, and D. Huang, "Quantitative optical coherence tomography angiography of vascular abnormalities in the living human eye," *Proceedings of the National Academy of Sciences of the United States of America*, vol. 112, pp. E2395-E2402, May 5 2015.

78. N. Zhang, T. H. Tsai, O. O. Ahsen, K. Liang, H. C. Lee, P. Xue, X. Li, and J. G. Fujimoto, "Compact piezoelectric transducer fiber scanning probe for optical coherence tomography," *Opt Lett*, vol. 39, pp. 186-8, Jan 15 2014.
79. Z. Wang, H. Jia, J. Tian, T. Soeda, R. Vergallo, Y. Minami, H. Lee, A. Aguirre, J. G. Fujimoto, and I. K. Jang, "Computer-aided image analysis algorithm to enhance in vivo diagnosis of plaque erosion by intravascular optical coherence tomography," *Circ Cardiovasc Imaging*, vol. 7, pp. 805-10, Sep 2014.
80. M.G. Giacomelli, Y. Sheikine, H. Vardeh, J.L. Connolly, and J.G. Fujimoto, "Rapid imaging of surgical breast excisions using direct temporal sampling two photon fluorescent lifetime imaging," *Biomed. Opt. Exp.* 6, 4317-4325, 2015.
81. W. Choi, E.M. Moulton, N.K. Waheed, M. Adhi, B. Lee, C.D. Lu, T.E. de Carlo, V. Jayaraman, P.J. Rosenfeld, J.S. Duker, and J.G. Fujimoto, "Ultrahigh-speed swept-source optical coherence tomography angiography in nonexudative age-related macular degeneration with geographic atrophy," *Ophthalmology* 122, 2532-2544, 2015.
82. W. R. Huang, E. A. Nanni, K. Ravi, K. H. Hong, L. J. Wong, P. D. Keathley, A. Fallahi, L. E. Zapata and F. X. Kärtner, "Toward a terahertz-driven electron gun," *Scientific Reports* 5, Article Number: 14899 (2015).
83. H. Liang, D. Weerawarne, P. Krogen, R. I. Grynko, C.-J. Lai, B. Shim, F. X. Kärtner, and K.-H. Hong, "Mid-infrared laser filaments in air at a kHz repetition rate," *Optica* 3, 678-681 (2016).
84. H. Liang, P. Krogen, K. Zawilski, P. Schunemann, F. X. Kärtner, and K.-H. Hong, "Phase-stable sub-single-cycle pulses from parametric amplification covering the entire range of 2.5 to 10 μm ," *OSA Congress on High-Brightness Sources 2016 (Long Beach, CA, Mar. 20-22, 2016), MICS/HILAS joint postdeadline paper JT3A.3.D.*
85. J. Fujimoto and E. Swanson, "The development, commercialization and impact of optical coherence tomography," *Invest. Ophthalmol. Vis. Sci.* 57, OCT1-OCT13, 2016.
86. M.G. Giacomelli, L. Husvagt, H. Vardeh, B.E. Faulkner-Jones, J. Hornegger, J.L. Connolly, and J.G. Fujimoto, "Virtual hematoxylin and eosin transillumination microscopy using epi-fluorescence imaging," *PLoS ONE* 11, e0159337, 2016.
87. H.-C. Lee, O.O. Ahsen, K. Liang, Z. Wang, C. Cleveland, L. Booth, B. Potsaid, V. Jayaraman, A.E. Cable, H. Mashimo, R. Langer, G. Traverso, and J.G. Fujimoto, "Circumferential optical coherence tomography angiography imaging of the swine esophagus using a micromotor balloon catheter," *Biomed. Opt. Exp.* 7, 2927-2942, 2016.
88. P. D. Keathley, S. Bhardwaj, J. Moses, G. Laurent, and F. X. K artner, "Volkov Transform Generalized Projection Algorithm for Attosecond Pulse Characterization," *New J. of Phys.* 18, 073009 (2016).

89. W. Choi, N.K. Waheed, E. Moulton, M. Adhi, B. Lee, T. De Carlo, V. Jayaraman, C.R. Baumal, J.S. Duker, and J.G. Fujimoto, "Ultra-high speed swept source optical coherence tomography of angiography of retinal and choriocapillaris alterations in diabetic patients with and without retinopathy," *Retina* (ePub August 2016).
90. G. J. Stein, P. D. Keathley, P. Krogen, H. Liang, J. P. Siqueira, C.-L. Chang, C.-J. Lai, K.-H. Hong, G. M. Laurent, and Franz X. Kärtner, "Water-window soft X-ray high-harmonic generation up to the nitrogen K-edge driven by a kHz, 2.1 μm OPCPA source," *J. Phys. B.: At. Mol. Opt. Phys.* 49, 155601 (2016).
91. W. R. Huang, A. Fallahi, X. Wu, H. Cankaya, A. L. Calendron, R. Koustuban, D. Zhang, E. A. Nanni, K.-H. Hong, and F. X. Kärtner, "Terahertz-driven, all-optical electron gun," *Optica* 3:(11) pp.1209-1212 (2016).
92. J. Schottenhamml, E. M. Moulton, S. Ploner, B. Lee, E. A. Novais, E. Cole, S. Dang, C. D. Lu, L. Husvogt, N. K. Waheed, J. S. Duker, J. Hornegger, and J. G. Fujimoto, "An Automatic, Intercapillary Area-Based Algorithm for Quantifying Diabetes-Related Capillary Dropout Using Optical Coherence Tomography Angiography," *Retina*, Sep 13 2016.
93. S. B. Ploner, E. M. Moulton, W. Choi, N. K. Waheed, B. Lee, E. A. Novais, E. D. Cole, B. Potsaid, L. Husvogt, J. Schottenhamml, A. Maier, P. J. Rosenfeld, J. S. Duker, J. Hornegger, and J. G. Fujimoto, "Toward Quantitative Optical Coherence Tomography Angiography: Visualizing Blood Flow Speeds in Ocular Pathology Using Variable Interscan Time Analysis," *Retina*, Sep 28 2016.
94. E. M. Moulton, N. K. Waheed, E. A. Novais, W. Choi, B. Lee, S. B. Ploner, E. D. Cole, R. N. Louzada, C. D. Lu, P. J. Rosenfeld, J. S. Duker, and J. G. Fujimoto, "Swept-Source Optical Coherence Tomography Angiography Reveals Choriocapillaris Alterations in Eyes with Nascent Geographic Atrophy and Drusen-Associated Geographic Atrophy," *Retina*, Sep 30 2016.
95. K. Liang, O. O. Ahsen, H. C. Lee, Z. Wang, B. M. Potsaid, M. Figueiredo, V. Jayaraman, A. E. Cable, Q. Huang, H. Mashimo, and J. G. Fujimoto, "Volumetric Mapping of Barrett's Esophagus and Dysplasia With en face Optical Coherence Tomography Tethered Capsule," *Am J Gastroenterol*, vol. 111, pp. 1664-1666, Nov 2016.
96. Z. Wang, B. Potsaid, L. Chen, C. Doerr, H. C. Lee, T. Nielson, V. Jayaraman, A. E. Cable, E. Swanson, and J. G. Fujimoto, "Cubic meter volume optical coherence tomography," *Optica*, vol. 3, pp. 1496-1503, Dec 20 2016.
97. T. Yoshitake, M. G. Giacomelli, L. C. Cahill, D. B. Schmolze, H. Vardeh, B. E. Faulkner-Jones, J. L. Connolly, and J. G. Fujimoto, "Direct comparison between confocal and multiphoton microscopy for rapid histopathological evaluation of unfixed human breast tissue," *J Biomed Opt*, vol. 21, p. 126021, Dec 01 2016.
98. H. Liang, P. Krogen, Z. Wang, H. Park, T. Kroh, K. Zawilski, P. Schunemann, J. Moses, F. X. Kärtner and K.-H. Hong, "High-energy mid-infrared sub-cycle pulse synthesis from a parametric

- amplifier,” *Nature Communications* 8, Article number: 141 (2017) doi:10.1038/s41467-017-00193-4.
99. W. P. Putnam, R. G. Hobbs, P. D. Keathley, K. K. Berggren and F. X. Kärtner, “Optical-field-controlled photoemission from plasmonic nanoparticles,” *Nat. Physics* 13. 335 (2017), doi:10.1038/nphys3978.
100. P. Krogen, H. Suchowski, H. Liang, N. Flemens, K.-H. Hong, F. X. Kärtner, and J. Moses, “Generation and Arbitrary Shaping of Intense Single-Cycle Pulses in the Mid-Infrared,” *Nature Photonics* 11, pp. 222–226 (2017).
101. K. Ravi and F. X. Kärtner, “Generating compressed broadband terahertz pulses using aperiodically poled electro-optic crystals,” arXiv:1710.07843 (2017).
102. E. A. Swanson and J. G. Fujimoto, "The ecosystem that powered the translation of OCT from fundamental research to clinical and commercial impact [Invited]," *Biomedical Optics Express*, vol. 8, pp. 1638-1664, Mar 1 2017.
103. E. M. Moulton, W. Choi, D. A. Boas, B. Baumann, A. C. Clermont, E. P. Feener, and J. G. Fujimoto, "Evaluating anesthetic protocols for functional blood flow imaging in the rat eye," *Journal of Biomedical Optics*, vol. 22, Jan 2017.
104. C. D. Lu, B. Lee, J. Schottenhamml, A. Maier, E. N. Pugh, Jr., and J. G. Fujimoto, "Photoreceptor Layer Thickness Changes During Dark Adaptation Observed With Ultrahigh-Resolution Optical Coherence Tomography," *Investigative ophthalmology & visual science*, vol. 58, pp. 4632-4643, 2017.
105. K. Liang, O. O. Ahsen, Z. Wang, H.-C. Lee, W. Liang, B. M. Potsaid, T.-H. Tsai, M. G. Giacomelli, V. Jayaraman, H. Mashimo, X. Li, and J. G. Fujimoto, "Endoscopic forward-viewing optical coherence tomography and angiography with MHz swept source," *Optics letters*, vol. 42, pp. 3193-3196, 2017.
106. H.-C. Lee, O. O. Ahsen, J. J. Liu, T.-H. Tsai, Q. Huang, H. Mashimo, and J. G. Fujimoto, "Assessment of the radiofrequency ablation dynamics of esophageal tissue with optical coherence tomography," *Journal of biomedical optics*, vol. 22, p. 76001, 2017.
107. H. C. Lee, O. O. Ahsen, K. Liang, Z. Wang, M. Figueiredo, M. G. Giacomelli, B. Potsaid, Q. Huang, H. Mashimo, and J. G. Fujimoto, "Endoscopic optical coherence tomography angiography microvascular features associated with dysplasia in Barrett's esophagus (with video)," *Gastrointest Endosc*, Feb 05 2017.
108. B. Lee, E. A. Novais, N. K. Waheed, M. Adhi, T. E. de Carlo, E. D. Cole, E. M. Moulton, W. Choi, M. Lane, C. R. Bauman, J. S. Duker, and J. G. Fujimoto, "En Face Doppler Optical Coherence Tomography Measurement of Total Retinal Blood Flow in Diabetic Retinopathy and Diabetic Macular Edema," *JAMA Ophthalmol*, vol. 135, pp. 244-251, Mar 01 2017.

109. U. Demirbas, J. Wang, G. S. Petrich, S. Nabanja, J. R. Birge, L. A. Kolodziejski, F. X. Kartner, and J. G. Fujimoto, "100-nm tunable femtosecond Cr:LiSAF laser mode locked with a broadband saturable Bragg reflector," *Applied Optics*, vol. 56, pp. 3812-3816, May 1 2017.
110. U. Demirbas, R. Uecker, J. G. Fujimoto, and A. Leitenstorfer, "Multicolor lasers using birefringent filters: experimental demonstration with Cr: Nd:GSGG and Cr:LiSAF," *Optics Express*, vol. 25, pp. 2594-2607, Feb 6 2017.
111. W. Choi, N. K. Waheed, E. M. Moul, M. Adhi, B. Lee, T. De Carlo, V. Jayaraman, C. R. Baumas, J. S. Duker, and J. G. Fujimoto, "Ultrahigh Speed Swept Source Optical Coherence Tomography Angiography of Retinal and Choriocapillaris Alterations in Diabetic Patients with and without Retinopathy," *Retina-the Journal of Retinal and Vitreous Diseases*, vol. 37, pp. 11-21, Jan 2017.
112. U. Demirbas, J. Wang, G. S. Petrich, S. Nabanja, J. R. Birge, L. A. Kolodziejski, F. X. Kartner, and J. G. Fujimoto, "100-nm tunable femtosecond Cr:LiSAF laser mode locked with a broadband saturable Bragg reflector," *Applied Optics*, vol. 56, pp. 3812-3816, May 1 2017.
113. T. Yoshitake, M. G. Giacomelli, L. M. Quintana, H. Vardeh, L. C. Cahill, B. E. Faulkner-Jones, J. L. Connolly, D. Do, and J. G. Fujimoto, "Rapid histopathological imaging of skin and breast cancer surgical specimens using immersion microscopy with ultraviolet surface excitation," *Sci Rep*, vol. 8, p. 4476, Mar 14 2018.
114. K. C. Liang, Z. Wang, O. O. Ahsen, H. C. Lee, B. M. Potsaid, V. Jayaraman, A. Cable, H. Mashimo, X. D. Li, and J. G. Fujimoto, "Cycloid scanning for wide field optical coherence tomography endomicroscopy and angiography in vivo," *Optica*, vol. 5, pp. 36-43, Jan 20 2018.
115. L. C. Cahill, M. G. Giacomelli, T. Yoshitake, H. Vardeh, B. E. Faulkner-Jones, J. L. Connolly, C. K. Sun, and J. G. Fujimoto, "Rapid virtual hematoxylin and eosin histology of breast tissue specimens using a compact fluorescence nonlinear microscope," *Lab Invest*, vol. 98, pp. 150-160, Jan 2018.
116. T. Kroh, C. Jin, P. Krogen, A.-L. Calendron, P. D. Keathley, J. P. Siqueira, H. Liang, E. L. Falcão-Filho, C. D. Lin, F. X. Kärtner and K.-H. Hong, "Enhanced high-harmonic generation up to the soft X-ray range driven by mid-IR pulses mixed with their third harmonic," *Optics Express* 26(13) 16955-16969 (2018)
117. Shih-Hsuan Chia, Phillip Keathley, William Putnam, Fabian Scheiba, Richard Hobbs, Karl Berggren, and Franz Kärtner. "Optical-Field-Controlled Photoemission from Plasmonic Nanoantennas with a Sub-Two-Cycle, 6 nJ, Octave-spanning Ti:sapphire Oscillator," submitted for publication (2018)
118. Phillip Keathley, William Putnam, Praful Vasireddy, Richard Hobbs, Karl Berggren, and Franz Kärtner. "Antiresonant-Like Behavior in Carrier-Envelope-Phase-Sensitive Sub-Optical-Cycle Photoemission from Plasmonic Nanoantennas." submitted for publication (2018)

119. William Putnam, Phillip Keathley, Richard Hobbs, Praful Vasireddy, Karl Berggren, and Franz Kärtner. "Sub-Cycle Effects in Carrier-Envelope-Phase-Sensitive Photoemission from Plasmonic Nanoparticles." submitted for publication (2018)
120. P. D. Keathley, W. P. Putnam, G. Laurent, L. F. Velasquez-García and F. X. Kärtner, "Re-Examining the Transition to Strong-Field Photoemission From Solids," submitted for publication (2018)

AFOSR Deliverables Submission Survey

Response ID:10138 Data

1.

Report Type

Final Report

Primary Contact Email

Contact email if there is a problem with the report.

ippen@mit.edu

Primary Contact Phone Number

Contact phone number if there is a problem with the report

617-253-8504

Organization / Institution name

MIT

Grant/Contract Title

The full title of the funded effort.

Advanced Photonics: Science, Technology and Applications

Grant/Contract Number

AFOSR assigned control number. It must begin with "FA9550" or "F49620" or "FA2386".

FA9550-12-1-0499

Principal Investigator Name

The full name of the principal investigator on the grant or contract.

Erich Ippen

Program Officer

The AFOSR Program Officer currently assigned to the award

Gernot Pomrenke

Reporting Period Start Date

10/01/2012

Reporting Period End Date

03/29/2018

Abstract

Progress over the five year period of this contract has been reported in five previous annual reports. The topics covered in those reports are listed at the on page 2.

The body of this report on pages 3-26 summarizes progress during the six month no-cost extension period 10/1/2017-3/29/2018. Topics include: Sub-cycle control of soft X-ray HHG yield using two-color ($\approx +3\pi$) driver pulses, Advances in nanostructured lightwave electronic devices, development of two-photon imaging technology for surgical imaging and optical biopsy and nonlinear microscopy (NLM) for histological evaluation.

A list of the 120 publication produced under this contract over the period 2013-2018 at the end on pages 27-36.

Distribution Statement

This is block 12 on the SF298 form.

Distribution A - Approved for Public Release
DISTRIBUTION A: Distribution approved for public release.

Explanation for Distribution Statement

If this is not approved for public release, please provide a short explanation. E.g., contains proprietary information.

SF298 Form

Please attach your [SF298](#) form. A blank SF298 can be found [here](#). Please do not password protect or secure the PDF. The maximum file size for an SF298 is 50MB.

[SF298_Form_-_lppen.pdf](#)

Upload the Report Document. File must be a PDF. Please do not password protect or secure the PDF. The maximum file size for the Report Document is 50MB.

[Final_Report_-_lppen_-_FA9550-12-1-0499.pdf](#)

Upload a Report Document, if any. The maximum file size for the Report Document is 50MB.

Archival Publications (published) during reporting period:

See also pp. 27-38 in Final Report

1. A. Khilo, S. J. Spector, M. E. Grein, A. H. Nejadmalayeri, Ch. W. Holzwarth, M. Y. Sander, M. S. Dahlem, M. Y. Peng, M. W. Geis, N. A. DiLello, J. U. Yoon, A. Motamedi, J. S. Orcutt, J. P. Wang, Ch. M. Sorace-Agaskar, M.A. Popović, J. Sun, G. R. Zhou, H. Byun, J. Chen, J. L. Hoyt, H. I. Smith, R. J. Ram, M. Perrott, Th. M. Lyszczarz, E. P. Ippen, and F. X. Kärtner, "Photonic ADC: overcoming the bottleneck of electronic jitter," *Opt. Express* 20:(4) 4454-4469 (2012).
2. W. Choi, B. Baumann, E.A. Swanson, and J.G. Fujimoto, "Extracting and compensating dispersion mismatch in ultrahigh-resolution Fourier domain OCT imaging of the retina," *Opt. Exp.* 20, 25357-25368, 2012
3. E. Granados, L-J. Chen, C-J. Lai, K-H. Hong, F. X. Kärtner, "Wavelength scaling of optimal hollow-core fiber compressors in the single-cycle limit," *Optics Express* 20:(8), pp.9099-9108 (2012).
4. D. Li, U. Demirbas, A. Benedick, A. Sennaroglu, J. G. Fujimoto and F. X. Kärtner, "Attosecond timing jitter pulse trains from semiconductor saturable absorber mode-locked Cr:LiSAF lasers," *Opt. Express* 20: (21), pp. 23422-23435 (2012).
5. W. P. Putnam, D. N. Schimpf, G. Abram, F. X. Kärtner, "Bessel-Gauss beam enhancement cavities for high-intensity applications", *Opt. Express* 20, 24429 (2012).
6. D. N. Schimpf, J. Schulte, W. P. Putnam, F. X. Kärtner, "Generalizing higher-order Bessel-Gauss beams: analytical description and demonstration", *Opt. Express* 20, 26852 (2012).
7. J. A. Cox, W. P. Putnam, A. Sell, A. Leitenstorfer, F. X. Kärtner, "Pulse synthesis in the single-cycle regime from independent mode-locked lasers using attosecond-precision feedback", *Opt. Lett.* 37, 3579 (2012).
8. I. Grulkowski, J.J. Liu, B. Potsaid, V. Jayaraman, C.D. Liu, J. Jiang, A.E. Cable, J.S. Duker, and J.G. Fujimoto, "Retinal, anterior segment and full eye imaging using ultrahigh speed swept source OCT with vertical-cavity surface emitting laser," *Biomed. Opt. Exp.* 3, 2733-2751, 2012
9. D. Keathley, A. Sell, W.P. Putnam, S. Guerrero, L. Velásquez-García, and F.X. Kärtner, "Strong-field photoemission from silicon field emitter arrays," *Ann. Phys.* 525:(1-2), 144-150 (2013).
10. J. Lim, H.-W. Chen, G. Chang, and F.X. Kärtner, "Frequency comb based on a narrowband Yb-fiber oscillator: pre-chirp management for self-referenced fCEO stabilization," *Opt Express.* 21:(4), 4531-4538 (2013).
11. S.-H. Huang, E. Granados, W. R. Huang, K.-H. Hong, L. E. Zapata and F. X. Kärtner, "High conversion efficiency, high energy terahertz pulses by optical rectification in cryogenically cooled lithium niobate," *Opt. Lett.* 38:(5), 796-798 (2013).
12. L. J. Wong, A. Fallahi and F. X. Kärtner, "Compact Electron Acceleration and Bunch Compression in THz Waveguides," *Opt. Express* 21, p. 9792 (2013).
13. W. Choi, B. Potsaid, V. Jayaraman, B. Baumann, I. Grulkowski, J.J. Liu, C.D. Lu, A.E. Cable, D. Huang, J.S. Duker, and J.G. Fujimoto, "Phase-sensitive swept-source optical coherence tomography imaging of the human retina with a vertical cavity surface-emitting laser light source," *Opt. Lett.* 38, 338-340, February 2013.
14. J.J. Liu, I. Grulkowski, M.F. Kraus, B. Potsaid, C.D. Lu, B. Baumann, J.S. Duker, J. Hornegger, and J.G. Fujimoto, "In vivo imaging of the rodent eye with swept source/Fourier domain OCT," *Biomed. Opt. Exp.* 4,

351-363, February 2013.

15. M. Y. Peng, P. T. Callahan, S. Valente, M. Xin, L. Grüner-Nielsen, E. Monberg, M. Yan, J. M. Fini, and F. X. Kärtner, "Sub-Femtosecond Timing Distribution via a 1.2-km Polarization-Maintaining Fiber Link: Approaching 10-21 Link Stability," *Opt. Exp.* 21:(17), 19982-19989 (2013).
16. I. Grulkowski, J.J. Liu, B. Potsaid, V. Jayaraman, J. Jiang, J.G. Fujimoto, and A.E. Cable, "High-precision, high-accuracy, ultralong-range swept-source optical coherence tomography using vertical cavity surface-emitting laser light source," *Opt. Lett.* 38, 673-675, March 2013.
17. W. R. Huang, S.W. Huang, E. Granados, R. Koustuban, K-H. Hong, L. E. Zapata, and F. X. Kärtner, "Highly efficiency THz pulse generation by optical rectification in stoichiometric and cryo-cooled congruent lithium niobate," *J. Mod. Optics* DOI:10.1080/09500340.2013.868547
18. S. Bhardwaj, S. K. Son, K.-H. Hong, C-J. Lai, F. X Kärtner, and R. Santra, "Recombination Amplitude of Noble Gases, in Length and Acceleration Form, beyond Strong Field Approximation," *Phys. Rev. A* 88, 053405 (2013).
19. X. Fu, K.-H. Hong, L.-J. Chen, and F. X. Kärtner, "Performance scaling of high-power picosecond cryogenically-cooled Yb:YAG multipass amplification," *J. Opt. Soc. Am. B* 30, 2798-2808 (2013).
20. A. Li, O.O. Ahsen, J.J. Liu, C. Du, M.L. McKee, W. Wasco, C.H. Newton-Cheh, C.J. O'Donnell, J.G. Fujimoto, C. Zhou, and R.E. Tanzi, "Silencing of the Drosophila ortholog of SOX5 in heart leads to cardiac dysfunction as detected by optical coherence tomography," *Hum. Mol. Gen.* 22, 3798-3806, (2013).
21. T-H. Tsai, B. Potsaid, Y.K. Tao, V. Jayaraman, J. Jiang, P.J.S. Heim, M.F. Kraus, C. Zhou, J. Hornegger, H. Mashimo, A.E. Cable, and J.G. Fujimoto, "Ultrahigh speed endoscopic optical coherence tomography using micromotor imaging catheter and VCSEL technology," *Biomed. Opt. Exp.* 4, 1119-1132, (2013).
22. C.-J. Lai, G. Cirmi, K.-H. Hong, J. Moses, S.W. Huang, E. Granados, P. Keathley, S. Bhardwaj, and F. X. Kärtner, "Wavelength scaling of high harmonic generation close to the multiphoton ionization regime," *Phys. Rev. Lett.* 111, 073901 (2013).
23. C. C. Evans, K. Shtyrkova, J.D.B. Bradley, O. Reshef, E. Ippen and E. Mazur, "Spectral broadening in anatase titanium dioxide waveguides at telecommunication and near-visible wavelengths," *Opt. Exp.*, 21, pp.18582-18591 (2013)
24. O.O. Ahsen, Y.K. Tao, B.M. Potsaid, Y. Sheikine, J. Jiang, I. Grulkowski, T-H. Tsai, V. Jayaraman, M.F. Kraus, J.L. Connolly, J. Hornegger, A. Cable, and J.G. Fujimoto, "Swept source optical coherence microscopy using a 1310 nm VCSEL light source," *Opt. Exp.* 21, 18021-18033, (2013).
25. H-C. Lee, J.J. Liu, Y. Sheikine, A.D. Aguirre, J.L. Connolly, and J.G. Fujimoto, "Ultrahigh speed spectral-domain optical coherence microscopy," *Biomed. Opt. Exp.* 4, 1236-1254, (2013).
26. D. N. Schimpf, W. P. Putnam, M.D.W Grogan, S. Ramachandran, and F.X. Kärtner, "Radially polarized Bessel-Gauss beams: decentered Gaussian beam analysis and experimental verification," *Optics Express*, Vol. 21 Issue 15, pp.18469-18483 (2013)
27. D. Keathley, A. Sell, W.P. Putnam, S. Guerrero, L. Velásquez-García, and F.X. Kärtner, "Strong-field photoemission from silicon field emitter arrays," *Ann. Phys.* 525:(1-2), 144-150 (2013).
28. S. P. Nabanja, L. A. Kolodziejski, G. S. Petrich, M. Y. Sander, J. L. Morse, K. Shtyrkova, E. P. Ippen and F. X. Kärtner, "Large-area broadband saturable Bragg reflectors using oxidized AIAs in the circular and inverted mesa geometries," *J. Appl. Phys.* 113, 163102 (2013)
29. H. Suchowski, P. R. Krogen, S.-W. Huang, F. X. Kärtner, and J. Moses, "Octave-spanning Coherent Mid-IR Generation via Adiabatic Difference Frequency Conversion," *Opt. Express* 21, 28892 (2013).
30. S. Carbajo, E. Granados, D. Schimpf, A. Sell, K.-H. Hong, J. Moses, and F. X. Kärtner, "Efficient generation of ultra-intense few-cycle radially polarized laser pulses." *Opt. Lett.* 39:(8), pp. 2487-2490 (2014).
31. A. Sell, and F. X. Kärtner, "Attosecond electron bunches accelerated and compressed by radially polarized laser pulses and soft-X-ray pulses from optical undulators," *J. Phys. B* 47, p. 015601 (2014), doi:10.1088/0953-4075/47/1/015601.
32. M. Adhi, J.J. Liu, A.H. Qavi, I. Grulkowski, J.G. Fujimoto, and J.S. Duker, "Enhanced visualization of choroido-scleral interface using swept-source OCT," *Ophthalmic Surg. Lasers Imaging Retina*, 44, S40-S42, November/December 2013.
33. I. Grulkowski, J.J. Liu, J.Y. Zhang, B. Potsaid, V. Jayaraman, A.E. Cable, J.S. Duker, and J.G. Fujimoto, "Reproducibility of a long-range swept-source optical coherence tomography ocular biometry system and

- comparison with clinical biometers," *Ophthalmology* 120, 2184-2190, November 2013
34. W. Choi, K.J. Mohler, B. Potsaid, C.D. Lu, J.J. Liu, V. Jayaraman, A.E. Cable, J.S. Duker, R. Huber, and J.G. Fujimoto, "Choriocapillaris and choroidal microvasculature imaging with ultrahigh speed OCT angiography," *PLOS One* 8, e81499, December 2013.
35. C.D. Lu, M.F. Kraus, B. Potsaid, J.J. Liu, W. Choi, V. Jayaraman, A.E. Cable, J. Hornegger, J.S. Duker, and J.G. Fujimoto, "Handheld ultrahigh speed swept source optical coherence tomography instrument using a MEMS scanning mirror," *Biomed. Opt. Exp.* 5, 293-311, January 2014.
36. M. Xin, K. Safak, M. Y. Peng, P. T. Callahan and F. X. Kärtner, "One-femtosecond, long-term stable remote laser synchronization over a 3.5-km fiber link," *Opt. Exp.* 22:(12) 14904 (2014). | DOI:10.1364/OE.22.014904.
37. M. E. Swanwick, P. D. Keathley, A. Fallahi, P. R. Krogen, G. Laurent, J. Moses, F. X. Kärtner, and L. F. Velásquez-García, "Nanostructured Ultrafast Silicon-Tip Optical Field-Emitter Arrays," *Nano Lett.*, 14:(9), pp 5035–5043 (2014).
38. R. Koustuban, W. R. Huang, S. Carbajo, X. Wu and F. X. Kärtner, "Limitations to THz generation by optical rectification using tilted pulse fronts," *Opt. Express* 22, 20239 (2014).
39. X. Wu, S. Carbajo, R. Koustuban, F. Ahr, G. Cirmi, Y. Zhou, O. D. Mücke and F. X. Kärtner, "Terahertz Generation in Lithium Niobate Driven by Ti:Sapphire Laser Pulses and its Limitations," *Opt. Lett.* 39: (18), pp. 5403-5406 (2014).
40. K. H. Hong, C. J. Lai, J. P. Siqueira, P. Krogen, J. Moses, C.-L. Chang, G. J. Stein, L. E. Zapata and F. X. Kärtner, "Multi-mJ, kHz, 2.1- μ m optical parametric chirped-pulse amplifier and high-flux soft X-ray high-harmonic generation," *Opt. Lett.* 39:(11), pp. 3145-3148 (2014).
41. M. Y. Peng, A. Kalaydzhyan, F. X. Kärtner, "Balanced optical-microwave phase detector for sub-femtosecond optical-RF synchronization," *Optics Express*, 22:(22) pp.27102-27111 (2014).
42. P. T. Callahan, K. Safak, P. Battle, T. D. Roberts, F. X. Kärtner, "Fiber-coupled balanced optical cross-correlator using PPKTP waveguides," *Optics Express* 22:(8), pp.9749-9758 (2014).
43. N. Zhang, T-H. Tsai, O.O. Ahsen, K. Liang, H.-C. Lee, P. Xue, X. Li, and J.G. Fujimoto, "Compact piezoelectric transducer fiber scanning probe for optical coherence tomography," *Opt. Lett.* 39, 186-188, January 2014.
44. J.G. Fein, L.A. Branchini, V. Manjunath, C.V. Regatieri, J.G. Fujimoto, and J.S. Duker, "Analysis of short-term change in subfoveal choroidal thickness in age-related macular degeneration using optical coherence tomography," *Ophthalmic Surg. Lasers Imaging Retina* 45, 32-37, January/February 2014.
45. A-L. Calendron, H. Çankaya, F. X. Kärtner, "High-energy kHz Yb:KYW dual-crystal regenerative amplifier," *Optics Express*, Vol. 22 Issue 20, pp.24752-24762 (2014).
46. D. Ferrara, K.J Mohler, N. Waheed, M. Adhi, J.J Liu, I. Grulkowski, M.F Kraus, C. Baumas, J. Hornegger, J.G Fujimoto, and J.S. Duker, "En face enhanced-depth swept-source optical coherence tomography features of chronic central serous chorioretinopathy," *Ophthalmology* 121, 719-726, March 2014.
47. T-H. Tsai, J.G. Fujimoto, and H. Mashimo, "Endoscopic optical coherence tomography for clinical gastroenterology," *Diagnostics* 4, 57-93, May 2014.
48. M. Adhi, J.J. Liu, A.H. Qavi, I. Grulkowski, C.D. Lu, K.J. Mohler, D. Ferrara, M.F. Kraus, C.R. Baumas, A.J. Witkin, N.K. Waheed, J. Hornegger, J.G. Fujimoto, and J.S. Duker, "Choroidal analysis in healthy eyes using swept-source optical coherence tomography compared to spectral domain optical coherence tomography," *Am. J. Ophthalmol.*, 157, 1272-1281, June 2014.
49. M.F. Kraus, J.J. Liu, J. Schottenhamm, C-L. Chen, A. Budai, L. Branchini, T. Ko, H. Ishikawa, G. Wollstein, J. Schuman, J.S. Duker, J.G. Fujimoto, and J. Hornegger, "Quantitative 3D-OCT motion correction with tilt & illumination correction, robust similarity measure and regulation," *Biomed. Opt. Exp.* 5, 2591-2613, July 2014.
50. J.J. Liu, A.J. Witkin, M. Adhi, I. Grulkowski, M.F. Kraus, A-H. Dhalla, C.D. Lu, J. Hornegger, J.S. Duker, and J.G. Fujimoto, "Enhanced vitreous imaging in healthy eyes using swept source optical coherence tomography," to *PLoS One* 9(7), e102950-1—10, July 2014.
51. Z. Wang, H-C. Lee, O.O. Ahsen, B. Lee, W. Choi, B. Potsaid, J. Liu, V. Jayaraman, A. Cable, M.F. Kraus, K. Liang, J. Hornegger, and J.G. Fujimoto, "Depth-encoded all-fiber swept source polarization sensitive OCT" *Biomed. Opt. Exp.* 5, 2931-2949, August 2014
52. T. Alasil, M. Adhi, J.J. Liu, J.G. Fujimoto, J.S. Duker, and C.R. Baumas, "Spectral-domain and swept-

- source OCT imaging of asteroid hyalosis: A case report," *Ophthalmic Surg. Lasers Imaging Retina* 45, 459-461, September/October 2014.
53. O.O. Ahsen, H-C. Lee, M.G. Giacomelli, Z. Wang, K. Liang, T-H. Tsai, B. Potsaid, H. Mashimo, and J.G. Fujimoto, "Correction of rotational distortion for catheter-based en face OCT and OCT angiography," *Opt. Lett.* 39, 5973-5976, October 2014.
54. Y.K. Tao, D. Shen, Y. Sheikine, O.O. Ahsen, H.H. Wang, D.B. Schmolze, N.B. Johnson, J.S. Brooker, A.E. Cable, J.L. Connolly, and J.G. Fujimoto, "Assessment of breast cancer pathologies using nonlinear microscopy," *Proc. Natl. Acad. Sci U.S.A.* 111, 15304-15309, October 2014.
55. M. Adhi, S.P. Read, J.J. Liu, J.G. Fujimoto and J.S. Duker, "High-speed ultrahigh-resolution OCT of Bruch's membrane in membranoproliferative glomerulonephritis type 2," *Ophthalmic Surg. Lasers Imaging Retina* 45, 614-617, November/December 2014.
56. E. Moults, W. Choi, N.K. Waheed, M. Adhi, B. Lee, C.D. Lu, V. Jayaraman, B. Potsaid, P.J. Rosenfeld, J.S. Duker, and J.G. Fujimoto, "Ultrahigh-Speed Swept-Source OCT Angiography in Exudative AMD," *Ophthalmic Surg. Lasers Imaging Retina* 45, 496-505, November/December 2014.
57. T-H. Tsai, H-C. Lee, O.O. Ahsen, K. Liang, M.G. Giacomelli, B.M. Potsaid, Y.K. Tao, V. Jayaraman, M. Figueiredo, Q. Huang, A.E. Cable, J.G. Fujimoto, and H. Mashimo, "Ultrahigh speed endoscopic optical coherence tomography for gastroenterology," *Biomed. Opt. Exp.*, 5, 4387-4404, November 2014.
58. T-H. Tsai, O.O. Ahsen, H-C. Lee, K. Liang, M. Figueiredo, Y.K. Tao, M.G. Giacomelli, B.M. Potsaid, V. Jayaraman, Q. Huang, A.E. Cable, J.G. Fujimoto, and H. Mashimo, "Endoscopic optical coherence angiography enables 3-dimensional visualization of subsurface microvasculature," *Gastroenterology* 4, 1219-1221, December 2014.
59. W. R. Huang, E. A. Nanni, A. Fallahi, P. D. Keathley, K. Ravi, K.H. Hong and Franz X. Kärtner, "An electron gun powered by single-cycle terahertz pulses, arXiv preprint arXiv:1409.8668 (2014)
60. R. Hobbs, Y. Yang, P. D. Keathley, M. E. Swanwick, L. F. Velasquez-Garcia, F. X. Kärtner, W. S. Graves, and K. K. Berggren, "High-density Au Nanorod Optical Field Emitter Arrays," *Nanotechnology*, 25, pp. 465304 – 465401 (2014).
61. K. Ravi, W. R. Huang, S. Carbajo, E. A. Nanni, D. N. Schimpf, E. P. Ippen and F. X. Kärtner, "Theory of terahertz generation by optical rectification using tilted-pulse-fronts," *Optics Express*, 23(4), 5253-5276 (2015)
62. K. Ravi, W. R. Huang, S. Carbajo, X. Wu and F. X. Kärtner, "Limitations to THz generation by optical rectification using tilted pulse fronts", *Optics Express*, 22(17),20239 (2014).
63. E. A. Nanni, W. R. Huang, K. H. Hong, K. Ravi, A. Fallahi, G. Moriena ,D. R. J. Miller and F. X. Kärtner, "Terahertz-driven linear electron acceleration", *Nature Communications* 6:8486 doi: 10.1038/ncomms9486 (2015).
64. X. Wu, S. Carbajo, K. Ravi, F. Ahr, G. Cirimi, Y. Zhou, O. D. Mücke and F. X. Kärtner, "Terahertz generation in lithium niobate driven by Ti:Sapphire laser pulses and its limitations", *Optics Letters*, 39(18), 5403 (2014)
65. O. Reshef, K. Shtyrkova, M.G. Moebius, S. Griesse-Nascimento, S. Spector C. C. Evans, E. P. Ippen, E. Mazur, "Polycrystalline anatase titanium dioxide microring resonators with negative thermo-optic coefficient," *JOSA B* 32(11) 2288-2293 (2015)
66. Kyung-Han Hong, Chien-Jen Lai, Jonathas Siqueira, Peter Krogen, Jeffrey Moses, Chun-Lin Chang, Gregory J. Stein, Luis E. Zapata, and Franz X. Kärtner, "Multi-mJ, kHz, 2.1- μ m optical parametric chirped pulse amplifier and high-flux soft X-ray high-harmonic generation," *Optics Letters* 39, 3145-3148 (June, 2014).
67. Cristian Manzoni, Oliver Mücke, Giovanni Cirimi, Shaobo Fang, Jeffrey Moses, Shu-Wei Huang, Kyung-Han Hong, Giulio Cerullo, Franz X. Kärtner, "Coherent pulse synthesis: towards sub-cycle optical waveforms (invited review)," *Laser and Photonics Reviews* 9, 129-171 (March, 2015).
68. Chun-Lin Chang, Peter Krogen, Houkun Liang, Gregory J. Stein, Jeffrey Moses, Chien-Jen Lai, Jonathas P. Siqueira, Lius E. Zapata, Franz X. Kärtner, and Kyung-Han Hong*, "Multi-mJ, kHz picosecond deep ultraviolet source," *Opt. Lett.* 40, 665 (Feb, 2015).
69. Houkun Liang, Peter Krogen, Ross Grynko, Ondrej Novak, Chun-Lin Chang, Gregory J. Stein, Darshana Weerawarne, Bonggu Shim, Franz X. Kärtner, and Kyung-Han Hong, "Three-octave-spanning supercontinuum generation and sub-two-cycle self-compression of mid-infrared filaments in dielectrics,"

Opt. Lett. 40, 106 (March, 2015).

70. Chun-Lin Chang, Peter Krogen, Kyung-Han Hong, Luis E. Zapata, Jeffrey Moses, Anne-Laure Calendron, Houkun Liang, Chien-Jen Lai, Gregory J. Stein, and Franz X. Kärtner, "High-energy, kHz, picosecond hybrid Yb-doped chirped-pulse amplifier," *Opt. Express* 23, 10132 (April, 2015).

71. Kyung-Han Hong, Chun-Lin Chang, Peter Krogen, Houkun Liang, Gregory J. Stein, Jeffrey Moses, Chien-Jen Lai, and Franz X. Kärtner, "Multi-mJ, kHz picosecond deep UV source based on a frequency-quadrupled cryogenic Yb:YAG laser," *Proc. of SPIE* 9513, High-Power, High-Energy, and High-Intensity Laser Technology II, 95130U (May, 2015).

72. Chien-Jen Lai, Kyung-Han Hong, Jonathas P. Siqueira, Peter Krogen, Chun-Lin Chang, Gregory J. Stein, Houkun Liang, Phillip D. Keathley, Guillaume Laurent, Jeffrey Moses, Luis E. Zapata, and Franz X. Kärtner, "Multi-mJ mid-infrared kHz OPCPA and Yb-doped pump lasers for tabletop coherent soft X-ray generation (invited)," *Journal of Optics* 17, 094009 (Sept, 2015).

73. Z. Wang, H. C. Lee, D. Vermeulen, L. Chen, T. Nielsen, S. Y. Park, A. Ghaemi, E. Swanson, C. Doerr, and J. Fujimoto, "Silicon photonic integrated circuit swept-source optical coherence tomography receiver with dual polarization, dual balanced, in-phase and quadrature detection," *Biomedical Optics Express*, vol. 6, pp. 2562-2574, Jul 1 2015.

74. K. Liang, G. Traverso, H. C. Lee, O. O. Ahsen, Z. Wang, B. Potsaid, M. Giacomelli, V. Jayaraman, R. Barman, A. Cable, H. Mashimo, R. Langer, and J. G. Fujimoto, "Ultrahigh speed en face OCT capsule for endoscopic imaging," *Biomed Opt Express*, vol. 6, pp. 1146-63, Apr 1 2015.

75. B. Lee, W. Choi, J. Liu, C. Lu, J. S. Schuman, G. Wollstein, J. S. Duker, N. Waheed, and J. G. Fujimoto, "Cardiac-Gated En Face Doppler Measurement of Retinal Blood Flow Using Swept Source Optical Coherence Tomography at 100,000 Axial Scans per Second," *Invest Ophthalmol Vis Sci*, vol. 56, pp. 2522-30, Apr 2015.

76. D. D. John, C. B. Burgner, B. Potsaid, M. E. Robertson, B. K. Lee, W. J. Choi, A. E. Cable, J. G. Fujimoto, and V. Jayaraman, "Wideband Electrically Pumped 1050-nm MEMS-Tunable VCSEL for Ophthalmic Imaging," *Journal of Lightwave Technology*, vol. 33, pp. 3461-3468, Aug 15 2015.

77. Y. L. Jia, S. T. Bailey, T. S. Hwang, S. M. McClintic, S. S. Gao, M. E. Pennesi, C. J. Flaxel, A. K. Lauer, D. J. Wilson, J. Hornegger, J. G. Fujimoto, and D. Huang, "Quantitative optical coherence tomography angiography of vascular abnormalities in the living human eye," *Proceedings of the National Academy of Sciences of the United States of America*, vol. 112, pp. E2395-E2402, May 5 2015.

78. N. Zhang, T. H. Tsai, O. O. Ahsen, K. Liang, H. C. Lee, P. Xue, X. Li, and J. G. Fujimoto, "Compact piezoelectric transducer fiber scanning probe for optical coherence tomography," *Opt Lett*, vol. 39, pp. 186-8, Jan 15 2014.

79. Z. Wang, H. Jia, J. Tian, T. Soeda, R. Vergallo, Y. Minami, H. Lee, A. Aguirre, J. G. Fujimoto, and I. K. Jang, "Computer-aided image analysis algorithm to enhance in vivo diagnosis of plaque erosion by intravascular optical coherence tomography," *Circ Cardiovasc Imaging*, vol. 7, pp. 805-10, Sep 2014.

80. M.G. Giacomelli, Y. Sheikine, H. Vardeh, J.L. Connolly, and J.G. Fujimoto, "Rapid imaging of surgical breast excisions using direct temporal sampling two photon fluorescent lifetime imaging," *Biomed. Opt. Exp.* 6, 4317-4325, 2015.

81. W. Choi, E.M. Moulton, N.K. Waheed, M. Adhi, B. Lee, C.D. Lu, T.E. de Carlo, V. Jayaraman, P.J. Rosenfeld, J.S. Duker, and J.G. Fujimoto, "Ultrahigh-speed swept-source optical coherence tomography angiography in nonexudative age-related macular degeneration with geographic atrophy," *Ophthalmology* 122, 2532-2544, 2015.

82. W. R. Huang, E. A. Nanni, K. Ravi, K. H. Hong, L. J. Wong, P. D. Keathley, A. Fallahi, L. E. Zapata and F. X. Kärtner, "Toward a terahertz-driven electron gun," *Scientific Reports* 5, Article Number: 14899 (2015).

83. H. Liang, D. Weerawarne, P. Krogen, R. I. Grynko, C.-J. Lai, B. Shim, F. X. Kärtner, and K.-H. Hong, "Mid-infrared laser filaments in air at a kHz repetition rate," *Optica* 3, 678-681 (2016).

84. H. Liang, P. Krogen, K. Zawilski, P. Schunemann, F. X. Kärtner, and K.-H. Hong, "Phase-stable sub-single-cycle pulses from parametric amplification covering the entire range of 2.5 to 10 μm ," *OSA Congress on High-Brightness Sources 2016* (Long Beach, CA, Mar. 20-22, 2016), MICS/HILAS joint postdeadline paper JT3A.3.D.

85. J. Fujimoto and E. Swanson, "The development, commercialization and impact of optical coherence tomography," *Invest. Ophthalmol. Vis. Sci.* 57, OCT1-OCT13, 2016.

86. M.G. Giacomelli, L. Husvagt, H. Vardeh, B.E. Faulkner-Jones, J. Hornegger, J.L. Connolly, and J.G. Fujimoto, "Virtual hematoxylin and eosin transillumination microscopy using epi-fluorescence imaging," *PLoS ONE* 11, e0159337, 2016.
87. H.-C. Lee, O.O. Ahsen, K. Liang, Z. Wang, C. Cleveland, L. Booth, B. Potsaid, V. Jayaraman, A.E. Cable, H. Mashimo, R. Langer, G. Traverso, and J.G. Fujimoto, "Circumferential optical coherence tomography angiography imaging of the swine esophagus using a micromotor balloon catheter," *Biomed. Opt. Exp.* 7, 2927-2942, 2016.
88. P. D. Keathley, S. Bhardwaj, J. Moses, G. Laurent, and F. X. Kärtner, "Volkov Transform Generalized Projection Algorithm for Attosecond Pulse Characterization," *New J. of Phys.* 18, 073009 (2016).
89. W. Choi, N.K. Waheed, E. Moulton, M. Adhi, B. Lee, T. De Carlo, V. Jayaraman, C.R. Baumal, J.S. Duker, and J.G. Fujimoto, "Ultrahigh speed swept source optical coherence tomography of angiography of retinal and choriocapillaris alterations in diabetic patients with and without retinopathy," *Retina* (epub August 2016).
90. G. J. Stein, P. D. Keathley, P. Krogen, H. Liang, J. P. Siqueira, C.-L. Chang, C.-J. Lai, K.-H. Hong, G. M. Laurent, and Franz X. Kärtner, "Water-window soft X-ray high-harmonic generation up to the nitrogen K-edge driven by a kHz, 2.1 μm OPCPA source," *J. Phys. B.: At. Mol. Opt. Phys.* 49, 155601 (2016).
91. W. R. Huang, A. Fallahi, X. Wu, H. Cankaya, A. L. Calendron, R. Koustuban, D. Zhang, E. A. Nanni, K.-H. Hong, and F. X. Kärtner, "Terahertz-driven, all-optical electron gun," *Optica* 3:(11) pp.1209-1212 (2016).
92. J. Schottenhamml, E. M. Moulton, S. Ploner, B. Lee, E. A. Novais, E. Cole, S. Dang, C. D. Lu, L. Husvagt, N. K. Waheed, J. S. Duker, J. Hornegger, and J. G. Fujimoto, "An Automatic, Intercapillary Area-Based Algorithm for Quantifying Diabetes-Related Capillary Dropout Using Optical Coherence Tomography Angiography," *Retina*, Sep 13 2016.
93. S. B. Ploner, E. M. Moulton, W. Choi, N. K. Waheed, B. Lee, E. A. Novais, E. D. Cole, B. Potsaid, L. Husvagt, J. Schottenhamml, A. Maier, P. J. Rosenfeld, J. S. Duker, J. Hornegger, and J. G. Fujimoto, "Toward Quantitative Optical Coherence Tomography Angiography: Visualizing Blood Flow Speeds in Ocular Pathology Using Variable Interscan Time Analysis," *Retina*, Sep 28 2016.
94. E. M. Moulton, N. K. Waheed, E. A. Novais, W. Choi, B. Lee, S. B. Ploner, E. D. Cole, R. N. Louzada, C. D. Lu, P. J. Rosenfeld, J. S. Duker, and J. G. Fujimoto, "Swept-Source Optical Coherence Tomography Angiography Reveals Choriocapillaris Alterations in Eyes with Nascent Geographic Atrophy and Drusen-Associated Geographic Atrophy," *Retina*, Sep 30 2016.
95. K. Liang, O. O. Ahsen, H. C. Lee, Z. Wang, B. M. Potsaid, M. Figueiredo, V. Jayaraman, A. E. Cable, Q. Huang, H. Mashimo, and J. G. Fujimoto, "Volumetric Mapping of Barrett's Esophagus and Dysplasia With en face Optical Coherence Tomography Tethered Capsule," *Am J Gastroenterol*, vol. 111, pp. 1664-1666, Nov 2016.
96. Z. Wang, B. Potsaid, L. Chen, C. Doerr, H. C. Lee, T. Nielson, V. Jayaraman, A. E. Cable, E. Swanson, and J. G. Fujimoto, "Cubic meter volume optical coherence tomography," *Optica*, vol. 3, pp. 1496-1503, Dec 20 2016.
97. T. Yoshitake, M. G. Giacomelli, L. C. Cahill, D. B. Schmolze, H. Vardeh, B. E. Faulkner-Jones, J. L. Connolly, and J. G. Fujimoto, "Direct comparison between confocal and multiphoton microscopy for rapid histopathological evaluation of unfixed human breast tissue," *J Biomed Opt*, vol. 21, p. 126021, Dec 01 2016.
98. H. Liang, P. Krogen, Z. Wang, H. Park, T. Kroh, K. Zawilski, P. Schunemann, J. Moses, F. X. Kärtner and K.-H. Hong, "High-energy mid-infrared sub-cycle pulse synthesis from a parametric amplifier," *Nature Communications* 8, Article number: 141 (2017) doi:10.1038/s41467-017-00193-4.
99. W. P. Putnam, R. G. Hobbs, P. D. Keathley, K. K. Berggren and F. X. Kärtner, "Optical-field-controlled photoemission from plasmonic nanoparticles," *Nat. Physics* 13, 335 (2017), doi:10.1038/nphys3978.
100. P. Krogen, H. Suchowski, H. Liang, N. Flemens, K.-H. Hong, F. X. Kärtner, and J. Moses, "Generation and Arbitrary Shaping of Intense Single-Cycle Pulses in the Mid-Infrared," *Nature Photonics* 11, pp. 222–226 (2017).
101. K. Ravi and F. X. Kärtner, "Generating compressed broadband terahertz pulses using aperiodically poled electro-optic crystals," arXiv:1710.07843 (2017).
102. E. A. Swanson and J. G. Fujimoto, "The ecosystem that powered the translation of OCT from fundamental research to clinical and commercial impact [Invited]," *Biomedical Optics Express*, vol. 8, pp.

1638-1664, Mar 1 2017.

103. E. M. Moulton, W. Choi, D. A. Boas, B. Baumann, A. C. Clermont, E. P. Feener, and J. G. Fujimoto, "Evaluating anesthetic protocols for functional blood flow imaging in the rat eye," *Journal of Biomedical Optics*, vol. 22, Jan 2017.
104. C. D. Lu, B. Lee, J. Schottenhamml, A. Maier, E. N. Pugh, Jr., and J. G. Fujimoto, "Photoreceptor Layer Thickness Changes During Dark Adaptation Observed With Ultrahigh-Resolution Optical Coherence Tomography," *Investigative ophthalmology & visual science*, vol. 58, pp. 4632-4643, 2017.
105. K. Liang, O. O. Ahsen, Z. Wang, H.-C. Lee, W. Liang, B. M. Potsaid, T.-H. Tsai, M. G. Giacomelli, V. Jayaraman, H. Mashimo, X. Li, and J. G. Fujimoto, "Endoscopic forward-viewing optical coherence tomography and angiography with MHz swept source," *Optics letters*, vol. 42, pp. 3193-3196, 2017.
106. H.-C. Lee, O. O. Ahsen, J. J. Liu, T.-H. Tsai, Q. Huang, H. Mashimo, and J. G. Fujimoto, "Assessment of the radiofrequency ablation dynamics of esophageal tissue with optical coherence tomography," *Journal of biomedical optics*, vol. 22, p. 76001, 2017.
107. H. C. Lee, O. O. Ahsen, K. Liang, Z. Wang, M. Figueiredo, M. G. Giacomelli, B. Potsaid, Q. Huang, H. Mashimo, and J. G. Fujimoto, "Endoscopic optical coherence tomography angiography microvascular features associated with dysplasia in Barrett's esophagus (with video)," *Gastrointest Endosc*, Feb 05 2017.
108. B. Lee, E. A. Novais, N. K. Waheed, M. Adhi, T. E. de Carlo, E. D. Cole, E. M. Moulton, W. Choi, M. Lane, C. R. Baumal, J. S. Duker, and J. G. Fujimoto, "En Face Doppler Optical Coherence Tomography Measurement of Total Retinal Blood Flow in Diabetic Retinopathy and Diabetic Macular Edema," *JAMA Ophthalmol*, vol. 135, pp. 244-251, Mar 01 2017.
109. U. Demirbas, J. Wang, G. S. Petrich, S. Nabanja, J. R. Birge, L. A. Kolodziejski, F. X. Kartner, and J. G. Fujimoto, "100-nm tunable femtosecond Cr:LiSAF laser mode locked with a broadband saturable Bragg reflector," *Applied Optics*, vol. 56, pp. 3812-3816, May 1 2017.
110. U. Demirbas, R. Uecker, J. G. Fujimoto, and A. Leitenstorfer, "Multicolor lasers using birefringent filters: experimental demonstration with Cr: Nd:GSGG and Cr:LiSAF," *Optics Express*, vol. 25, pp. 2594-2607, Feb 6 2017.
111. W. Choi, N. K. Waheed, E. M. Moulton, M. Adhi, B. Lee, T. De Carlo, V. Jayaraman, C. R. Baumal, J. S. Duker, and J. G. Fujimoto, "Ultrahigh Speed Swept Source Optical Coherence Tomography Angiography of Retinal and Choriocapillaris Alterations in Diabetic Patients with and without Retinopathy," *Retina-the Journal of Retinal and Vitreous Diseases*, vol. 37, pp. 11-21, Jan 2017.
112. U. Demirbas, J. Wang, G. S. Petrich, S. Nabanja, J. R. Birge, L. A. Kolodziejski, F. X. Kartner, and J. G. Fujimoto, "100-nm tunable femtosecond Cr:LiSAF laser mode locked with a broadband saturable Bragg reflector," *Applied Optics*, vol. 56, pp. 3812-3816, May 1 2017.
113. T. Yoshitake, M. G. Giacomelli, L. M. Quintana, H. Vardeh, L. C. Cahill, B. E. Faulkner-Jones, J. L. Connolly, D. Do, and J. G. Fujimoto, "Rapid histopathological imaging of skin and breast cancer surgical specimens using immersion microscopy with ultraviolet surface excitation," *Sci Rep*, vol. 8, p. 4476, Mar 14 2018.
114. K. C. Liang, Z. Wang, O. O. Ahsen, H. C. Lee, B. M. Potsaid, V. Jayaraman, A. Cable, H. Mashimo, X. D. Li, and J. G. Fujimoto, "Cycloid scanning for wide field optical coherence tomography endomicroscopy and angiography in vivo," *Optica*, vol. 5, pp. 36-43, Jan 20 2018.
115. L. C. Cahill, M. G. Giacomelli, T. Yoshitake, H. Vardeh, B. E. Faulkner-Jones, J. L. Connolly, C. K. Sun, and J. G. Fujimoto, "Rapid virtual hematoxylin and eosin histology of breast tissue specimens using a compact fluorescence nonlinear microscope," *Lab Invest*, vol. 98, pp. 150-160, Jan 2018.
116. T. Kroh, C. Jin, P. Krogen, A.-L. Calendron, P. D. Keathley, J. P. Siqueira, H. Liang, E. L. Falcão-Filho, C. D. Lin, F. X. Kärtner and K.-H. Hong, "Enhanced high-harmonic generation up to the soft X-ray range driven by mid-IR pulses mixed with their third harmonic," *Optics Express* 26(13) 16955-16969 (2018)
117. Shih-Hsuan Chia, Phillip Keathley, William Putnam, Fabian Scheiba, Richard Hobbs, Karl Berggren, and Franz Kärtner. "Optical-Field-Controlled Photoemission from Plasmonic Nanoantennas with a Sub-Two-Cycle, 6 nJ, Octave-spanning Ti:sapphire Oscillator," submitted for publication (2018)
118. Phillip Keathley, William Putnam, Praful Vasireddy, Richard Hobbs, Karl Berggren, and Franz Kärtner. "Antiresonant-Like Behavior in Carrier-Envelope-Phase-Sensitive Sub-Optical-Cycle Photoemission from Plasmonic Nanoantennas." submitted for publication (2018)
119. William Putnam, Phillip Keathley, Richard Hobbs, Praful Vasireddy, Karl Berggren, and Franz Kärtner.

"Sub-Cycle Effects in Carrier-Envelope-Phase-Sensitive Photoemission from Plasmonic Nanoparticles."
submitted for publication (2018)

120. P. D. Keathley, W. P. Putnam, G. Laurent, L. F. Velasquez-Garcia and F. X. Kärtner, "Re-Examining the
Transition to Strong-Field Photoemission From Solids," submitted for publication (2018)

New discoveries, inventions, or patent disclosures:

Do you have any discoveries, inventions, or patent disclosures to report for this period?

No

Please describe and include any notable dates

Do you plan to pursue a claim for personal or organizational intellectual property?

Changes in research objectives (if any):

None

Change in AFOSR Program Officer, if any:

Program begun under Howard Schlossberg.

Extensions granted or milestones slipped, if any:

A 6-month no-cost-extension was approved at the end of the 5-year program.

AFOSR LRIR Number

LRIR Title

Reporting Period

Laboratory Task Manager

Program Officer

Research Objectives

Technical Summary

Funding Summary by Cost Category (by FY, \$K)

	Starting FY	FY+1	FY+2
Salary			
Equipment/Facilities			
Supplies			
Total			

Report Document

Report Document - Text Analysis

Report Document - Text Analysis

Appendix Documents

2. Thank You

E-mail user

Jul 30, 2018 16:08:18 Success: Email Sent to: ippen@mit.edu